CHAPTER 5

COLLECTIVE EFFECTS

5.1 INTRODUCTION

Collective effects, arising from the electromagnetic interaction of the beam particles among themselves, with their environment (possibly including 'foreign particles' such as electrons) and with the other beam, will ultimately limit the performance of the LHC. Depending on the beam intensity and on the bunch filling pattern, they give rise to parasitic losses, can cause beam instabilities or degrade the beam quality by emittance growth and poor lifetime of all or some specific bunches. A first summary of collective effects in the LHC was presented in [1], a systematic review of single beam effects can be found in [2], and intermediate reviews have been published in [3, 4, 5, 6, 7, 8, 9].

Collective effects include incoherent phenomena, concerning the behaviour of a single particle in the electromagnetic field produced by all the others, and coherent interactions of the beam with its surroundings, usually described in terms of coupling impedances. The LHC impedance budget is discussed in the next Section and a review of single-beam instability mechanisms is presented in Sec. 5.3. Cures against instabilities, discussed in Sec. 5.4, include feedback systems, chromaticity control, and Landau damping of the coherent beam oscillation modes, that takes place providing their tune shifts remain within the incoherent tune spread. Landau damping can be considered as a bridge between incoherent and coherent phenomena.

Examples of incoherent effects are direct space charge and Laslett tune shifts due to image currents, as well as residual gas and intra-beam scattering (IBS). The latter are discussed in Sec. 5.5, which contains a summary of the mechanisms leading to emittance growth. As discussed in [2], the magnetic Laslett tune shift at injection in the LHC is about 1.7×10^{-2}: this large tune shift, having opposite sign in the two betatron planes, can be compensated by adjusting the tuning quadrupoles. Effects associated with the incoherent synchrotron radiation are presented in Sec. 5.6. Coherent effects include parasitic losses, summarized in Sec. 5.7, and complex tune shifts of the beam oscillation modes.

Seed electrons created by ionization of the residual gas at injection or photo-electrons liberated by the large number of hard U.V. synchrotron radiation photons at 7 TeV are pulled towards the positively charged LHC proton bunches. When they hit the opposite wall, they generate secondary electrons which can in turn be accelerated by the next bunch if they are slow enough to survive. This mechanism can lead to the fast build-up of an *electron cloud*, discussed in Sec. 5.8, with potential implications for beam stability, emittance growth, and heat load on the cold beam screen. Electron cloud effects have been actively investigated at CERN since 1997 by analytic estimates, simulations, and experiments [10, 11, 12].

Beam-beam effects are discussed in Sec. 5.9. They include incoherent effects, such as betatron tune spreads associated with the nonlinear head-on and long range collisions as well as a reduction of dynamic aperture for insufficient beam separation at the parasitic encounters, and coherent effects affecting orbit, tunes, and chromaticities of the different bunches (depending on their different collision schedules) or coherent oscillation modes. The effect of long range beam-beam encounters can be compensated by electro-magnetic lenses [13], which are being experimentally investigated, and the luminosity can be optimized by increasing bunch length or crossing angle [14].

5.2 IMPEDANCE BUDGET

Single-bunch collective effects are associated with the broad-band impedance of low-Q structures, discussed in [8], while multi-bunch effects are dominated by the narrow-band impedance of high-Q resonators [9]. The narrow-band nature of the transverse resistive wall impedance at low frequency also leads to coupled-bunch instabilities.

5.2.1 Narrow-Band Impedance of High-Q Resonators

Detailed tables of damped and undamped higher order modes (HOM's) for 400 MHz and 200 MHz RF cavities, transverse damper system, and trapped modes in the CMS vacuum chamber can be found in [9].

5.2.2 Transverse Resistive Wall Impedance

In the LHC, about 90% of the circumference will be maintained at 5 to 20 K while the remaining 10% of the circumference will be at room temperature and will be generally equipped with a 2 mm thick copper beam pipe. The cryogenic part of the LHC beam pipe (mainly beam screen) will be copper cladded stainless steel to keep the resistance as low as possible both for instability and ohmic heating considerations. The resistivity of the cold copper is a function of the residual resistance ratio (RRR) and of the magnetic field B. The magnetic field increases the path length of the conduction electrons which leads to a substantial resistance increase at cryogenic temperatures. The final resistivity depends more on the field than on the RRR for very high magnetic fields. Past experience with co-laminating stainless steel with copper showed that the copper close to the steel gets contaminated during the fabrication process such that the surface impedance is increased. The increase of the resistance has been compensated by increasing the thickness of the copper layer from 50 to 75 μm. The equivalent thickness and RRR at low-B turn out to be 50 μm and 100, respectively, whereas the RRR reduces to 30 at high B [9]. The Yokoya factors [15] for the LHC beam screen geometry are derived from a geometry halfway between square and elliptical. Since the dimensions a and b of the beam screen in the two planes satisfy $(a-b)/(a+b) = 0.1$, vertical and horizontal Yokoya factors $Y_{\rm V} = 0.87$ and $Y_{\rm H} = 0.63$, respectively are assumed.

Tab. 5.1 gives the values of the transverse resistive wall impedance for each major LHC component, excluding collimators that will be treated separately. For easy comparison of the different components, the transverse impedance is normalised by a weighting factor $\beta/\langle\beta\rangle$, where β is the local betatron function in the relevant H or V plane, estimated based on LHC optics version 6.2, and $\langle\beta\rangle = 70$ m the average β-function defined as the ratio R/Q of the average machine radius to the betatron tune. These impedance estimates include the effect of the so-called inductive by-pass [16] and the Yokoya factors for non-cylindrical components. The 'effective' resistive wall impedances reported in Tab. 5.1 refer to the first slow wave at 8 kHz, corresponding to a non-integer part of the betatron tune equal to about 0.3, and to the slow wave at 20 MHz, corresponding to the frequency bandwidth of the transverse feedback system. The contributions at higher harmonics of the 40 MHz bunch frequency for these slow waves have been taken into account for the kickers and the TDI. It should be pointed out that for an easy comparison of the different impedance sources, including the collimators discussed in the next section, the sum over the higher harmonics of the coupled-bunch rigid mode spectrum is not normalized by the corresponding sum of the spectral densities. The resulting 'effective' impedance differs from the usual definition [17] by a factor $s_{\rm b}/2\sqrt{\pi}\sigma_z$, depending on the ratio of the bunch spacing $s_{\rm b}$ to the r.m.s. bunch length σ_z, and equal to about 28 for the LHC at 7 TeV. With this definition the coherent tune shifts[1] of the coupled-bunch modes are given by $\Delta Q = j\langle I\rangle\langle\beta\rangle Z_\perp^{\rm eff}/4\pi(E/e)$, where $\langle I\rangle$ is the *average* rather than the peak beam intensity.

The MQW and MBW are special types of magnets in the cleaning insertions. The MBW magnets have a circular chamber of radius 0.022 m. The MQW magnets have an elliptical chamber with $(a-b)/(a+b) = 0.275$ and an inscribed radius of 0.0145 m. The corresponding Yokoya factors are 0.85 and 0.5. Half of the major axes are in the horizontal plane, the other half in the vertical plane, following the value of the optical function β. The total resistive wall impedance is about equal in both planes for these magnet chambers and can be found with sufficient accuracy by assuming an average Yokoya factor of 0.7 and an average value for β.

The TDI is a special 'collimator' to be used for protecting the machine from a potential misfiring of the injection kickers. A thin 3 μm layer of Ti is assumed. The Yokoya factors are $\pi^2/12$ and $\pi^2/24$. The effect of the inductive by-pass is large due to the high surface impedance. As a consequence the contribution of the harmonics of the 40 MHz bunch frequency is relatively important.

Interconnects are the assemblies that contain the shielded bellows. The longitudinal resistance for one unit

[1] Oscillations are considered to be of the form $\exp(jQ\omega_o t)$, where $j = -i$ and ω_o is the revolution frequency. Therefore a beam instability corresponds to a coherent tune shift ΔQ with negative imaginary part and to an effective impedance with negative real part.

Table 5.1: Transverse resistive wall (low-frequency) impedance for the LHC without collimators. The first four columns report element name, latest relevant reference, total length in m and inner radius b in mm. The last two columns give the transverse 'effective' impedance $Z_\perp^{\rm eff}$ in MΩ/m for the slow waves at 8 kHz and at 20 MHz multiplied by $\beta/\langle\beta\rangle$, where $\langle\beta\rangle = 70$ m.

element	Ref.	length	b	$Z_\perp^{\rm eff}$ [8 kHz]	$Z_\perp^{\rm eff}$ [20 MHz]
		m	mm	MΩ/m	MΩ/m
Beam screen-H @low *B*	[9]	23600	22	-21.4+6.3j	-1+0.3j
Beam screen-V @low *B*	[9]	23600	18	-29.5+8.6j	-1.5+0.5j
Beam screen-H @high *B*	[9]	23600	22	-61+7.2j	-3+0.3j
Beam screen-V @high *B*	[9]	23600	18	-84.4+9.9j	-4+0.5j
Interconnects	[19]	340	22	-5.3+0.5j	-
Cold-warm transitions		10	22	-0.6+0.3j	-
Warm pipe (pipe+etc.)		2400	40	-3.5+2.9j	-0.2+0.2j
MQW (2 mm Cu)		155	14.5	-4.3+4.8j	-0.3+0.3j
MQW (2 mm SS)		5		-1.4+1.6j	-0.1+0.1j
MBW (2 mm Cu)		70	22	-0.6+0.6j	-0.05+0.05j
MBW (2 mm SS)		2		-0.21+0.18j	-
TDI-H @injection		2.8		-	-0.8+4.5j
TDI-V @injection		2.8	5	-	-0.5+3j
Injection-Septum-H	[20]	22	22	-0.3	-
Injection-Septum-V	[20]	22		-0.5+0.1j	-
Dump-Septum	[20]	72	25	-1.3+0.2j	-
Injection-Kicker-H	[21]	15	19	-0.4+4j	-
Dump-Kicker-V		22.5	29	-1+5j	0+7.2j

with length 0.2 m is 100 $\mu\Omega$. For the cold-warm transitions, RRR=10 for the 3 μm thick copper layer, owing to pollution from SS are assumed.

The injection kickers are equipped with 5 μm thick Cu stripes covering 1/2 of the ceramic chamber. This is equivalent to a solid coating by a 2.5 μm thick copper layer [22]. The same remarks on the effect of inductive by-pass and 40 MHz harmonics as for the TDI apply for the injection and dump kickers.

The total resistive wall impedance at injection and at top energy, excluding collimators, is summarized in Tab. 5.2 for the slow waves at 8 kHz and 20 MHz. Most of this impedance depends on frequency as $1/\sqrt{\omega}$.

Table 5.2: LHC transverse resistive wall impedance budget in MΩ/m (no collimators).

	horizontal	vertical
TOTAL $Z_\perp^{\rm eff}$ @injection, 8 kHz slow wave	-40+22j	-49+26j
TOTAL $Z_\perp^{\rm eff}$ @injection, 20 MHz slow wave	-3+6j	-3+12j
TOTAL $Z_\perp^{\rm eff}$ @top energy, 8 kHz slow wave	-79+22j	-103+26j
TOTAL $Z_\perp^{\rm eff}$ @top energy, 20 MHz slow wave	-5+1j	-5+8j

Resistive wall impedance of the collimators

The impedance for a single graphite collimator has been estimated analytically and numerically in [16, 17]. The thick-wall approximation with 'inductive by-pass' has been used, since even at the lowest frequency around 8 kHz for the first slow wave the skin depth in graphite is about 2 cm and thus smaller than the 2.5 cm thickness of the collimator block. The corresponding analytic expression for a single collimator in [16] with a half-gap of 2 mm yields results in excellent agreement with the numerical results obtained using the code HFSS in [17]. A thin Cu coating of about 1 μm thickness would considerably reduce the real part of the coherent tune shift [17, 18] and improve beam stability, as discussed in Sec. 5.4.5. However such a thin coating may not

survive during machine operation.

The collimator scheme considered here corresponds to the baseline design described in Chap. 18 and including graphite collimators at all reserved spaces (some of which will not be installed for the LHC start-up), with 20 collimators in IR7 and 7 collimators in IR3 having lengths of 20 cm for the 5 primary collimators and 1 m for the 22 secondary collimators[2]. The β-functions at the collimators range from 27 m to 360 m and the range of collimator half-gaps is 4.7 to 11.1 mm for the injection optics and 1.2 to 3.8 mm for the squeezed optics. For our impedance estimate no metallic coating, a carbon jaw resistivity $\rho = 14 \times 10^{-6}\,\Omega$m, and continuity of the electric contact with the beam pipe are assumed. The corresponding 'effective' resistive wall impedance is reported in Tab. 5.3 for the slow waves at 8 kHz and at 20 MHz. At injection the real part of the collimator impedance has a mild maximum around 0.2 MHz, while for the squeezed optics at 7 TeV the maximum is around 1 MHz. The 'effective' impedances for the corresponding most critical coupled-bunch modes are $(-11 + 55j)$ MΩ/m and $(-100 + 1400j)$ MΩ/m, respectively. The real part of the impedance for a single collimator varies approximately with $\sqrt{\omega}$ below the maximum and with $1/\sqrt{\omega}$ for frequencies well above the maximum. The frequency corresponding to the maximum of $\mathrm{Re}(Z_\perp)$ depends on ρ/b^2. The imaginary part of the impedance at low frequency tends to a constant value proportional to $1/b^2$. Also the maximum of $\mathrm{Re}(Z_\perp)$ is proportional to $1/b^2$.

Table 5.3: Vertical 'effective' impedance of the LHC collimators, normalized to $\langle\beta\rangle = 70$ m, for un-coated Carbon jaws with resistivity $\rho = 14 \times 10^{-6}\,\Omega$m. The effect of the inductive bypass, of the Yokoya coefficients, and the contribution at higher harmonics of the 40 MHz bunch frequency for the slow waves at 8 kHz and at 20 MHz have been properly taken into account.

	$Z_\perp^{\mathrm{eff}}$ [8 kHz]	$Z_\perp^{\mathrm{eff}}$ [20 MHz]
	MΩ/m	MΩ/m
injection optics	-7.6+74j	33j
squeezed optics	-42+1800j	-7.2+1160j

5.2.3 Broad-Band Impedance

Several elements contribute to the LHC broad-band impedance [8] and Tab. 5.4 gives a list of the corresponding effective longitudinal and transverse impedance, the latter being normalized to $\langle\beta\rangle = 70$ m. Roman pots (see the Glossary) are assumed retracted and shielded.

For the BPM's a 0.5 mm slit between electrode and body is assumed. The 'monitor' inductance per electrode is 4 pH, the 'slit' inductance 9 pH, and the 'cavity' inductance 4 pH, giving a total of about 60 pH or $Z/n = j\,4.2\,\mu\Omega$/monitor. 500 monitors, including some overhead for special and warm BPM's are considered.

The 1700 shielded bellows have a depth of 5 mm on 20 mm radius, corresponding to an inductance of 81 pH. 350 vacuum valves having an inner radius of 31.5 mm, a chamber radius of 40 mm and sloping edges at 15°, corresponding to an inductance of 0.2 nH per valve are considered.

The experimental chambers have inductances of 7.3 nH (CMS), 13.2 nH (Alice), 117 nH (LHCb), $75 \div 100$ nH (vertex detector), and 15 nH for the rest of the IP. The total inductance is therefore 140 nH.

The shunt impedance for a 400 MHz cavity unit is $R/Q = 44.5\,\Omega$. Thus the total inductance for 8 units is 144 nH. The effective inductance is somewhat smaller. The shunt impedance for a 200 MHz cavity unit is $R/Q = 192\,\Omega$ and the total inductance for 4 units is therefore 600 nH, corresponding to $Z/n = j\,0.045\,\Omega$. The effective inductance is only a fraction of this, which is estimated at one third. The transverse impedance of the RF cavities is not included in the total broad-band impedance, since it does not extend beyond ≈ 1 MHz, while most of the remaining impedance extends up to about 5 GHz, corresponding to the cut-off frequency of the vacuum chamber.

The inductance of each of the 8 recombination chambers (Y-chambers) is 1.5 nH. Total length of the unshielded bellows is 2.6 m (0.36 m in Alice, 0.6 m in CMS, 0.75 m in ATLAS, and 0.9 m in LHCb) giving an

[2]The present baseline for Phase 1 includes only 4 primary and 15 secondary collimators per beam and the impedance is therefore somewhat reduced.

Table 5.4: LHC broad-band impedance budget. The first three columns report element name, latest relevant reference, and inner vertical aperture b in mm. The last two columns give the effective longitudinal and transverse impedance in the vertical plane, the latter being multiplied by $\beta/\langle\beta\rangle$, where $\langle\beta\rangle = 70\,\mathrm{m}$.

element	Ref.	b	Im(Z/n)	Im$(Z_\perp)$
		mm	Ω	MΩ/m
Pumping slots	[23]	18	0.017	0.5
BPM's	[24]	25	0.0021	0.3
Unshielded bellows		25	0.0046	0.06
Shielded bellows		20	0.010	0.265
Vacuum valves		40	0.005	0.035
Experimental chambers		-	0.010	-
RF Cavities (400 MHz)		150	0.010	(0.011)
RF Cavities (200 MHz)		50	0.015	(0.155)
Y-chambers (8)	[25]	-	0.001	-
BI (non-BPM instruments)		40	0.001	0.012
space charge @injection	[2]	18	-0.006	0.02
Collimators @injection optics		$4.4 \div 8$	0.0005	0.15
Collimators @squeezed optics		$1.3 \div 3.8$	0.0005	1.5
TOTAL broad-band @injection optics			0.070	1.34
TOTAL broad-band @squeezed optics			0.076	2.67

inductance of 65 nH.

24 BI instruments per ring other than BPM's, with inner radius of 0.04 m, outer radius 0.06 m, and sloping edges are assumed. This gives a total inductance of 12 nH. Special components like injection and dump kickers, septa and TDI are not expected to contribute significantly to the longitudinal impedance budget, since they are equipped with a thin metallic layer on their inner surface. Also the inductance of the beam screen sawtooth surface is negligible [26].

Space Charge Impedance

As discussed in [27], the transverse coherent tune of rigid dipole beam oscillations is not affected by the direct space charge effect. For a round beam with uniform density, one can formally define a direct space charge impedance giving rise to a collective tune shift which is compensated by the incoherent space charge tune shift $\Delta Q_{\perp,sc}^{\mathrm{inc}} = -\frac{N_\mathrm{b} r_\mathrm{p}}{4\pi B\beta\gamma^2\varepsilon_\mathrm{n}}$. Here N_b is the number of protons per bunch, r_p the classical proton radius, B the bunching factor, $\gamma = (1-\beta^2)^{-1/2}$ the Lorentz factor, and $\varepsilon_\mathrm{n} = \beta\gamma\varepsilon$ the normalized transverse beam emittance. Following Chao [28], the transverse space charge impedance can be written $Z_\perp = -j\,\frac{Z_0 R}{\beta^2\gamma^2}\left(\frac{1}{2a^2} - \frac{1}{b^2}\right)$. It has a direct effect, corresponding to a large capacitive contribution inversely proportional to the square of the average beam radius $a = \sqrt{\varepsilon\langle\beta\rangle}$, and a much smaller inductive contribution from the image currents on the beam pipe of radius b. Only the latter has been reported in Tab. 5.4, since the real tune shift induced by the direct space charge impedance for rigid dipole oscillations of a beam with *non uniform* transverse distribution i) is compensated by the incoherent tune shift for particles with small betatron amplitudes and ii) is unlikely to give rise to coherent instabilities thanks to the direct space charge tune spread for particles with larger betatron amplitudes (see also [29] and the discussion at the end of Sec. 5.4.4).

At injection energy, the incoherent space charge tune shift for nominal LHC bunch intensity is -1.36×10^{-3} and the direct space charge impedance is $-j\,6.35\,\mathrm{M}\Omega/\mathrm{m}$. At 7 TeV these values become -7×10^{-6} and $-j\,0.41\,\mathrm{M}\Omega/\mathrm{m}$, respectively.

Geometric Impedance of the Collimators

In the LHC the bunches are long and the collimator gaps after the β-squeeze are narrow. In addition the collimators are tapered at a small angle θ. (Wake fields for un-tapered collimators were computed in [30] and [31].) Therefore this is a regime, where $kb\theta \ll 1$ is fulfilled. For an ultra-relativistic particle, the wave number k is related to the frequency ω via $k = \omega/c$, and the maximum bunch frequency is of order c/σ_z. The above condition can be re-written as:

$$b\theta/\sigma_z \ll 1.$$

For example, with $\sigma_z = 7\,\text{cm}$, $b = 2.5\,\text{mm}$, and $\theta = 0.35$, the left side is 0.13, so that the inequality is still fulfilled.

The impedance of a round collimator for this regime was computed by Yokoya [32] and Stupakov [33]. The transverse impedance is:

$$Z_\perp = j\,\frac{Z_0}{2\pi}\int_{-\infty}^{\infty}\left(\frac{b'}{b}\right)^2 dz,$$

where $b = b(z)$ describes the evolution of the beam pipe aperture with longitudinal position and $b(-\infty) = b(\infty)$ is assumed.

If the beam passes the collimator with an offset y from the center of the collimator gap, it receives a centroid kick:

$$\Delta y' = \frac{N_\mathrm{b} r_\mathrm{p}}{\gamma}\kappa_\perp y,$$

where the coefficient $\kappa_\perp$ is the loss factor (or kick factor):

$$\kappa_\perp = -\frac{1}{\pi}\int_0^\infty d\omega |\tilde{f}(\omega)|^2 \mathrm{Im}Z_\perp(\omega),$$

and $\tilde{f}$ is the Fourier transform of the normalized longitudinal charge distribution (for a Gaussian $\tilde{f} = \exp(-\sigma_z^2\omega^2/(2c^2))$.

Considering the two sides of a tapered collimator and assuming that the collimator gap b is much narrower than the surrounding beam pipe, the loss factor is:

$$\kappa_\perp = \frac{2\theta}{\sqrt{\pi}\sigma_z}\frac{1}{b}.$$

For our example above, this evaluates to about 3000. An important parameter is the normalized deflection or jitter enhancement factor:

$$C \equiv \frac{\beta\Delta y'}{\Delta y} = \frac{\beta N_\mathrm{b} r_\mathrm{p}}{\gamma}\kappa_\perp.$$

Using the above numbers, and also $N_\mathrm{b} \approx 10^{11}$, $\beta = 200\,\text{m}$, $\gamma \approx 7500$, gives $C \approx 10^{-5}$. This number applies to a single collimator with half-gap $b = 2.5\,\text{mm}$. The corresponding impedance is $j\,\theta Z_0/(\pi b)$ or $j16.8\,\text{k}\Omega/\text{m}$. The broad-band impedance for 21 collimator units reported in Tab. 5.4 for the squeezed optics has been estimated by multiplying this value by a factor ≈ 2 to account for the weighted β-functions and by an additional safety factor of 2, in view of somewhat larger inductances obtained for similar tapered structures [24]. The impedance at injection is estimated to be 10 times lower. Further numerical estimates of the geometric collimator impedance are ongoing.

5.3 SINGLE-BEAM CONVENTIONAL INSTABILITY MECHANISMS

In this section rise times and thresholds for different single-beam conventional instabilities are reviewed. The imaginary part of the effective impedance is responsible for (real) coherent tune shifts and can lead to collective instabilities owing to mode coupling or to loss of Landau damping, while a negative real part of the effective impedance is related to the instability rise time.

5.3.1 Single-bunch coherent tune shifts

At injection with nominal LHC single bunch intensity, the inductive broad-band impedance summarized in Tab. 5.4 induces a transverse real coherent tune shift of the rigid ($m = 0$) mode $\Delta Q^{(0)}_{\perp,bb} = -1.7 \times 10^{-4}$. For the first few higher order head-tail modes of order m this tune shift is divided by $m + 1$. Similarly, at 7 TeV with squeezed optics and collimators in closed position $\Delta Q^{(0)}_{\perp,bb} = -3.82 \times 10^{-5}$.

5.3.2 Multi-bunch coherent tune shifts and resistive wall instability

The coherent tune shifts of coupled-bunch modes induced by the narrow-band impedance of damped and undamped HOM's for 400 MHz and 200 MHz RF cavities, transverse damper system, and trapped modes in the CMS vacuum chamber are listed in [9].

At injection, the vertical resistive wall 'effective' impedance for the slow wave at 8 kHz is $(-49+26j)$ MΩ/m plus $(-7.6+74j)$ MΩ/m for the collimators[3], giving a total of $(-56.6+100j)$ MΩ/m. The corresponding tune shift for a nominal LHC bunch population of 1.15×10^{11} protons, assuming a uniform machine filling with 3564 bunches, is $\Delta Q_{\rm V} = -(9.1 + 5.2j) \times 10^{-4}$. The vertical resistive wall instability rise time for the most unstable rigid coupled-bunch mode is therefore $1/(2\pi\,{\rm Im}(\Delta Q_{\rm V})) \simeq 308$ turns or 27.4 ms. For ultimate LHC beam intensity, corresponding to a bunch population of 1.7×10^{11} protons, the instability rise time becomes 208 turns or 18.5 ms.

5.3.3 Mode-coupling and microwave instability thresholds

The total broad-band longitudinal impedance $Z/n = j\,0.07\,\Omega$ at injection or $Z/n = j\,0.076\,\Omega$ at top energy is significantly lower than originally assumed in [2, 5]. The threshold single bunch intensity for loss of Landau damping of the longitudinal single-bunch modes at 7 TeV is about 9×10^{11} protons per bunch, well above the nominal and ultimate LHC bunch intensity, while the threshold for the longitudinal microwave instability is two orders of magnitude above the nominal LHC bunch intensity.

Similarly, the total transverse broad-band impedance is $j\,1.34$ MΩ/m at injection and $j\,2.67$ MΩ/m at 7 TeV. These values are lower than the transverse effective impedance assumed in [2, 8] and the transverse mode-coupling instability threshold at injection is now above 2×10^{12} protons per bunch. Mode-coupling for multi-bunch modes may occur at somewhat lower beam intensities, as discussed in [3] for an earlier impedance model. A systematic revision of all single- and multi-bunch effects with an updated LHC impedance model, including a detailed frequency dependence of the narrow and broad-band impedance and based on a dedicated impedance data-base [34], is taking place at the time of writing.

5.4 CURES AGAINST INSTABILITIES

5.4.1 HOM damping and controlled emittance blow-up

To ensure longitudinal stability at injection for nominal LHC beam intensity with a longitudinal emittance of 0.7 eVs, the shunt impedance of all the HOM's in high-Q cavity-like structures should be limited to 60 kΩ in the frequency range $100 \div 500$ MHz. The limitation for the shunt impedance then increases with frequency as $f_r^{5/3}$. As discussed in [7], a controlled emittance blow-up proportional to $\sqrt{E}$ is sufficient to avoid degradation of the longitudinal beam stability during acceleration to 7 TeV.

5.4.2 Transverse feedback system

A transverse feedback system is required to damp coupled-bunch instabilities caused by the narrow-band impedance, and in particular the resistive wall instability, at injection and during acceleration to 7 TeV. Since the feedback system can only dump rigid ($m = 0$) head-tail modes, higher order head-tail modes have to be stabilized by Landau damping or (slightly) negative chromaticity. On the other hand, operation with the

[3] This is a somewhat conservative estimate corresponding to an intermediate collimator layout.

transverse feedback and large betatron tune spread may lead to a significant emittance growth [35] and should be avoided. Therefore the LHC strategy is to switch off the feedback system before the end of the energy ramp and to ensure Landau damping of *all* the head-tail modes by proper control of the tune spread using the arc octupoles.

5.4.3 Tune spread: Landau damping octupoles and beam-beam

In addition to octupolar spool-pieces for the local b_4 correction of the superconducting dipoles, in the LHC arcs there are two families of magnetic octupoles to control the betatron detuning with amplitude and provide Landau damping of the coherent beam oscillation modes. The horizontal and vertical betatron functions at the 84 focusing octupoles are $\beta_{\rm x}^{\rm OF} = 180\,{\rm m}$ and $\beta_{\rm y}^{\rm OF} = 30\,{\rm m}$, respectively, and these values are swapped at the 84 defocusing octupoles. Each octupole has a magnetic length of 0.32 m and a maximum integrated strength $O_3 = 59100\,{\rm T\,m^{-3}}$. The amplitude-dependent incoherent horizontal tune can be written $Q_{\rm x} = Q_o + aJ_{\rm x} + bJ_{\rm y}$, where $J_{\rm x}$ and $J_{\rm y}$ are the betatron action variables. The maximum value of the anharmonicities is $a = 270000\,{\rm m^{-1}}$ and $b = -175420\,{\rm m^{-1}}$, with $c = b/a = -0.65$. Given the nominal beam emittance at 7 TeV $\varepsilon = 0.5\,{\rm nm}$, the corresponding maximum detuning at $1\,\sigma$ rms is $\Delta Q_{1\,\sigma} = a\varepsilon = 1.35 \times 10^{-4}$ in each plane. Landau damping for a pseudo-parabolic betatron distribution with $J_{\rm x} + J_{\rm y} \leq 5\sigma^2$, as discussed in [36, 37] is assumed. This is a somewhat conservative assumption, valid for a scraped beam with no tails beyond $3.2\,\sigma$. The corresponding stability curves at 7 TeV are shown in Fig. 5.1 for positive or negative values of the maximum anharmonicity a. Potentially unstable oscillation modes with negative imaginary tune shifts are stabilized by Landau damping provided their coherent tune shifts remain below these stability curves. It is interesting to remark that for real tune shifts, such as those induced by the broad-band impedance, modes with a maximum (negative) tune shift about 3.5 times the detuning at $1\,\sigma$ are still Landau damped. The tune spread associated with long range beam-beam encounters provides an additional (modest) stabilizing effect [38].

5.4.4 Coherent tune shifts and Landau damping at injection

As seen in Sec. 5.3.1, at injection the transverse coherent tune shifts of the single-bunch higher order head-tail modes with $m > 0$ are smaller than or equal to 0.85×10^{-4} in absolute value. The natural nonlinearities of the magnetic lattice still compatible with an adequate dynamic aperture correspond to a maximum detuning of 2×10^{-3} at $6\,\sigma$ [39], *i.e.*, about 0.56×10^{-4} at $1\,\sigma$. This provides Landau damping of coherent modes having real tune shifts up to about 3.5 times larger, corresponding to an effective tune spread of nearly 2×10^{-4}. Therefore all the single-bunch head-tail modes with $m > 1$ are Landau damped by the lattice nonlinearities, if these are pushed to the limit. The rigid $m = 0$ head-tail mode will be damped by the feedback system. In case the lattice nonlinearities need to be reduced to guarantee a sufficient dynamic aperture, the direct space charge tune spread of about 10^{-3} will provide additional Landau damping of the higher-order head tail modes[4].

5.4.5 Coherent tune shifts and Landau damping at 7 TeV after β-squeeze

The tune shift of the most unstable rigid coupled bunch mode at top energy is $-(0.13+0.42j)\times10^{-4}$ without collimators. The maximum tune shift induced by uncoated graphite collimators is $-(7.45+0.55j)\times10^{-4}$ and that induced by graphite collimators with 1μm Cu coating, assuming a resistivity $\rho_{\rm Cu} = 1.5 \times 10^{-8}\,\Omega{\rm m}$, is $-(2.83 + 0.84j) \times 10^{-4}$. Fig. 5.1 (left) shows the situation for the nominal LHC beam at 7 TeV without collimators and including collimators (either coated or uncoated), taking as an upper bound the sum of the maximum tune shifts. Also the small real tune shift $\Delta Q^{(0)}_{\perp,bb} = -4\times10^{-5}$ induced by the broad-band impedance has been added in all cases. The conclusion is that Landau damping may not be ensured, even for copper coated collimators: the upgraded, low-impedance collimation scheme described in Chap. 18 is needed to reach and exceed nominal LHC performance. For the baseline collimator design without copper coating, stability is

[4]This assumption needs experimental validation in the regime of the LHC at injection energy, where the space charge tune spread is somewhat larger than the tune spread associated with the natural nonlinearities of the magnetic lattice. Observations at the CERN PS with very long bunches and space charge detunings much larger than those associated with the lattice nonlinearities indicate that the direct space charge tune spread may not be effective in providing Landau damping of the higher-order transverse head-tail modes [29].

ensured up to about 40% of the nominal beam intensity, as shown in Fig. 5.1 (right), and up to about 65% of the nominal beam intensity for copper coated collimators.

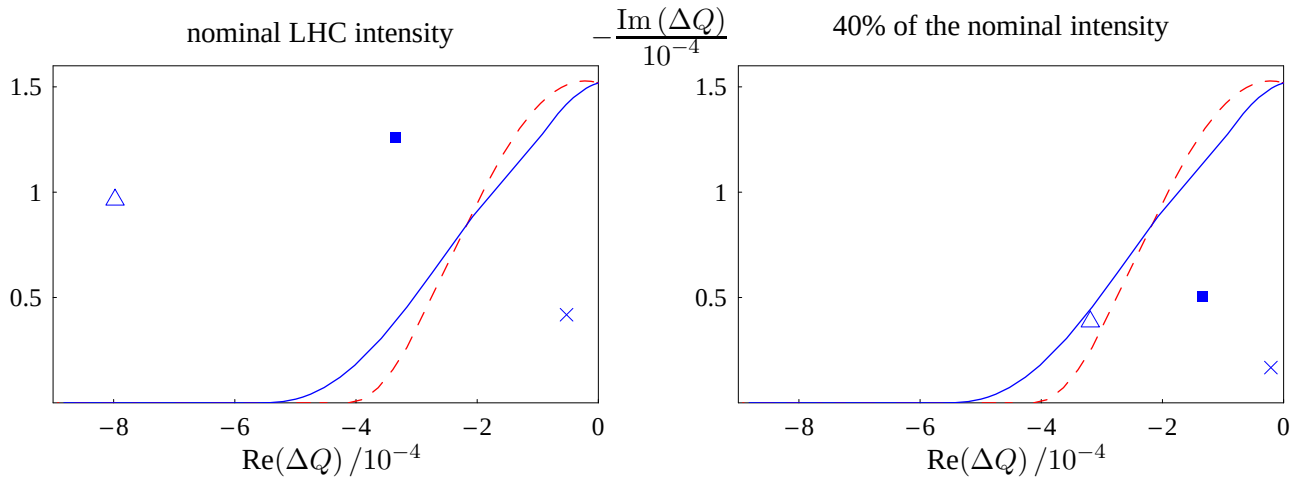

Figure 5.1: Stability limits for a detuning $\Delta Q_{1\,\sigma} = \pm 1.35 \times 10^{-4}$ and coherent tune shifts for the LHC at 7 TeV with squeezed optics and nominal LHC beam intensity (left) or 40% of the nominal intensity (right). The horizontal and vertical axes give the real part and minus the imaginary part, respectively, of the coherent tune shift for the most unstable coupled bunch rigid mode ($m = 0$): without collimators (cross), with copper coated graphite collimators (square), and with un-coated graphite collimators (triangle) at $\beta^* = 0.5\,\mathrm{m}$. The dashed (red) curve is the stability limit for maximum Landau octupole current with negative anharmonicity $a < 0$, the solid (blue) curve with positive anharmonicity $a > 0$.

5.5 SUMMARY OF EMITTANCE GROWTH AND BEAM LOSS MECHANISMS

5.5.1 Emittance growth caused by transverse injection oscillations

The effective overall damping time τ_{damp} of the LHC damper has to be significantly shorter than the decoherence time τ_{dec} of the injection oscillations to preserve the transverse emittance. For injection oscillations corresponding to a maximum transverse offset Δx, the relative emittance blow-up is given by [35]:

$$\frac{\Delta\sigma^2}{\sigma^2} \simeq \frac{1}{2}\,\frac{\Delta x^2/\sigma^2}{\left(1+\frac{\tau_{\mathrm{dec}}}{\tau_{\mathrm{damp}}}\right)^2}.$$

The LHC damping time for low intensity beams is 40 turns, corresponding to about 3.6 ms. At higher beam intensities, the damping rate is reduced by the resistive wall instability growth rate $1/\tau_{\mathrm{inst}}$, leading to an overall damping rate:

$$\frac{1}{\tau_{\mathrm{damp}}} = \frac{1}{40\,\mathrm{turns}} - \frac{1}{\tau_{\mathrm{inst}}}.$$

At nominal LHC beam intensity, the instability rise time is $\tau_{\mathrm{inst}} = 308$ turns and the overall damping time of the injection oscillations is 46 turns, corresponding to about 4.1 ms. After correction of the lattice nonlinearities at injection, it is thought that it is possible to reach a decoherence time around 750 turns, or 67 ms, corresponding to a full tune spread of about 1.3×10^{-3}. Assuming a maximum injection offset $\Delta x = 4\,\mathrm{mm}$, a modest emittance blow-up of about 1.9% is estimated.

At ultimate LHC beam intensity, the resistive wall instability rise time is $\tau_{\mathrm{inst}} = 208$ turns, or 18.5 ms, and the overall damping time of the injection oscillations becomes about 50 turns, or 4.4 ms. The corresponding emittance blow-up is 2.2%, i.e. still below 2.5%.

5.5.2 Intra-Beam Scattering

Small-angle particle-particle collisions within a bunch couple the horizontal and longitudinal particle oscillations and, above transition energy, give rise to an irreversible emittance growth in both planes. The horizontal IBS growth rate is approximately proportional to the particle density in the six-dimensional phase space. For nominal LHC beam parameters at top energy, the longitudinal IBS emittance growth time is 63 h and the horizontal growth time is 105 h. These values have been computed with the Bjorken-Mtingwa formalism implemented in MAD [40] for the LHC collision optics version 6.4.

The evolution of the LHC beam emittance during a physics store at 7 TeV is discussed in [41] and a plot including the effect of intra-beam scattering, particle consumption at the two high-luminosity IP's, and radiation damping is shown in Fig. 5.3.

5.5.3 Touschek Scattering

Touschek scattering refers to particle-particle collisions within a bunch, through which enough energy is transferred from transverse into longitudinal oscillations that the scattered particles leave the stable RF bucket. The loss rate due to Touschek scattering is quadratic in the bunch population and has been estimated for the LHC in [42]. For nominal beam parameters, coasting beam is produced at a rate per proton of $1.8 \times 10^{-4}\,\mathrm{h}^{-1}$ during injection and $8 \times 10^{-5}\,\mathrm{h}^{-1}$ at 7 TeV.

Once the protons are outside the RF bucket, they lose energy due to synchrotron radiation. If the collimators provide an energy aperture of 3.9×10^{-3}, a scattered proton is lost after about 390 hours at injection or after 6.5 minutes at top energy, respectively. While the energy drift due to synchrotron radiation is unimportant at injection, at 7 TeV it gives rise to a steady-state coasting beam component of about 10^{-5}.

5.5.4 Residual Gas Scattering

Residual-gas molecules reduce the proton beam lifetime due to nuclear scattering and they increase the beam emittance by multiple elastic Coulomb scattering. For the first time in an accelerator, beam loss due to the nuclear scattering represents a non-negligible heat load on the cold bore of the magnets. In consequence, a minimum beam lifetime of 100 h has been required, so as to ensure that the heat load due to nuclear scattering stays below 0.1 W/m for the two beams [43]. The beam lifetime τ is related to the cross section σ and gas density n via $1/\tau = c\sigma n$. Tab. 5.5 lists cross sections and the implied maximum allowed molecule densities for various gas species. Most of the cross sections were taken from [44]. The highest density of $1.2 \times 10^{15}\,\mathrm{m}^{-3}$ is permitted for hydrogen, corresponding to a 38-ntorr pressure at room temperature. The dipole magnet quench limit of 7×10^6 p/m/s at 7 TeV corresponds to a gas density about two orders of magnitude higher (see [45], p. 70).

The normalized emittance growth due to multiple scattering is:

$$\frac{d(\gamma\epsilon)}{dt} = \bar{\beta}\gamma \left(\frac{13.6\ \mathrm{MeV}}{\beta cp}\right)^2 \frac{cnm_{gas}}{X_0}\ ,$$

where m_{gas} is the mass of a molecule, X_0 the radiation length in units of $\mathrm{kg\,m}^{-3}$, and $\bar{\beta}$ the average beta function ($\bar{\beta} \approx 100$ m at injection, and $\bar{\beta} \approx 150$ m at top energy). The effect of multiple scattering is largest at injection. Emittance growth times expected at 450 GeV for the partial gas pressures corresponding to a 100 h nuclear-scattering lifetime are also included in Tab. 5.5. The emittance e-folding times are seen to range from 5 to 15 h, depending on the gas species. After some conditioning of the vacuum system, it is expected a fractional gas composition with less than 5% CO and CO_2 molecules. The emittance growth times will therefore be dominated by H_2.

5.5.5 Emittance Dilution caused by Collimators and Electron Cloud

If the beam passes a collimator with an offset y from the center of the collimator gap, it receives a centroid kick and an additional differential deflection along the bunch, which for a round collimator can be computed

Table 5.5: Nuclear scattering cross sections, the implied maximum allowed densities, and the accompanying emittance growth at injection for various gas species.

molecule	σ [barn] at 7 TeV	n [m^{-3}] at 7 TeV for $\tau_{\rm nucl} = 100$ h	equiv. gas pressure at 300 K [ntorr]	τ_ϵ [h] at 450 GeV for $\tau_{\rm nucl} = 100$ h
H_2	0.078	1.2×10^{15}	37.8	17.0
He	0.133	6.9×10^{14}	21.7	12.5
CH_4	0.511	1.8×10^{14}	5.6	7.6
H_2O	0.510	1.8×10^{14}	5.7	9.5
CO	0.751	1.2×10^{14}	3.8	7.5
CO_2	1.171	7.9×10^{13}	2.5	5.0

from the wake field:

$$w_\perp(s) = -\frac{j}{2\pi}\int_s^\infty \frac{e^{-s'^2/(2\sigma_z^2)}}{\sqrt{2\pi}\sigma_z}\int_{-\infty}^{\infty} d\omega e^{j(s-s')\omega/c} Z_\perp(\omega) = \frac{4\theta}{b}\frac{e^{-s^2/(2\sigma_z^2)}}{\sqrt{2\pi}\sigma_z},$$

where θ is the tapering angle and b the collimator gap. The rms spread of the kick (direct emittance growth) is $\sqrt{2}\sqrt{1/\sqrt{3}-1/2} \approx 0.4$ times smaller than the centroid kick. In other words, for a $1\,\sigma$ offset at the collimator, the beam emittance would blow up by 5×10^{-6}, so that after 2×10^5 turns it would be doubled, if the emittance growth were additive from turn to turn: this hypothesis needs further beam dynamics studies.

Considering a rigid oscillation or static displacement from the center of amplitude y, the deflection experienced by a particle at position s along the bunch passing the collimator is:

$$\Delta y'(s) = y\frac{N_b r_p}{\gamma} w_\perp(s).$$

For a flat collimator, a further emittance dilution arises from the quadrupole wake, which blows up the beam, even if the latter is perfectly centered between the jaws. This problem has also been studied by Stupakov [46]. In this case, the impedance depends on the offset of the local centroid (y_s) and the test particle (y_t), at the same longitudinal location. The generalized deflection under the condition that $\sigma_z \gg h^2\theta/b$ is [47]:

$$\Delta y'_t = \frac{\lambda_s r_p}{\gamma}\left(\frac{4\theta}{b}y_s - \frac{4\theta}{b}y_t + \frac{2\pi\theta h}{b^2}y_t\right),$$

where h is the half width of the beam pipe in the orthogonal transverse plane, and λ_s the local line density.

Preliminary results concerning the emittance growth caused by the electron cloud are discussed in Sec. 5.8.5. A quantitative estimate of the emittance dilution caused by collimators and electron cloud requires further investigations.

5.6 SYNCHROTRON RADIATION

The LHC is the first proton storage ring for which synchrotron radiation becomes a noticeable effect. At top energy, the synchrotron radiation gives rise to a significant heat load, which is intercepted by a beam screen at an elevated temperature of 5–20 K. The synchrotron radiation also leads to a shrinkage of the beam emittance during physics stores. Pertinent parameters are summarized in Tab. 5.6.

5.6.1 Photon Flux and Heat Load

Each of the two LHC beams emits 1.8×10^{21} photons per second, or on average 6.8×10^{16} photons per second and per metre of the ring. The proton energy loss per turn is 6.7 keV, at 7 TeV. The corresponding total power radiated per beam is 3886 W, with an average critical photon energy of 43.13 eV [48].

In the arcs, the average number of photons amounts to 8.2×10^{16} photons incident per metre length, second and beam. The synchrotron radiation power per metre bend and per beam is 0.22 W/m. In the long straight

Table 5.6: Synchrotron Radiation

parameter	450 GeV	7 TeV
total power / beam	0.066 W	3886 W
energy loss per turn	0.11 eV	6.7 keV
average photon flux per metre and second	0.4×10^{16}	6.8×10^{16}
photon critical energy	0.01 eV	43.13 eV
longit. emittance damping time	5.5 yr	12.9 h
transv. emittance damping time	11 yr	26 h

sections the average flux on the wall is 20 times smaller than in the arcs, or about 3.6×10^{15} photons per metre per second, as is illustrated in Fig. 5.2.

On the other hand, at injection energy, the synchrotron radiation stays negligible, with a total radiated power of only 0.066 W and a proton energy loss per turn of 0.11 eV.

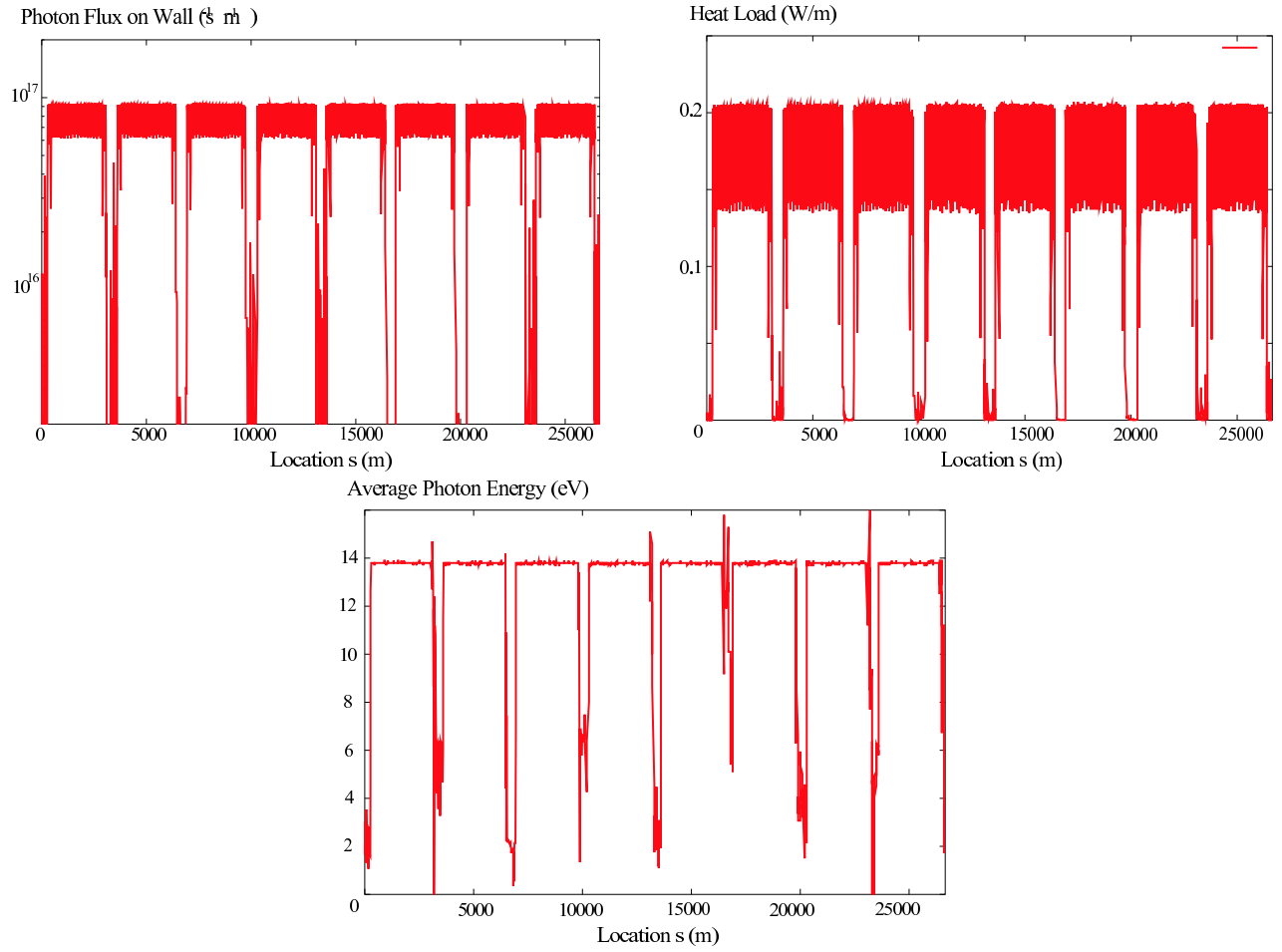

Figure 5.2: Synchrotron radiation as a function of position around the LHC: photon flux on wall per metre and per second (top left), heat load in W/m (top right), and average photon energy in eV (bottom) [48].

5.6.2 Emittance Damping

The synchrotron radiation gives rise to a continuous shrinkage of the beam emittances with exponential emittance-damping times of 26.0 h in the two transverse planes and 12.9 h in the longitudinal plane, at 7 TeV. The damping times scale with the inverse third power of the beam energy. For example, the damping is ten times weaker at 3.25 TeV. The damping times vary only by 1–2%, when either the crossing angles are turned

off or large optics errors are introduced.

In collision, due to the shrinkage of the emittance, the LHC luminosity decays less strongly than exponentially. The radiation damping may also compensate for emittance dilution due to other processes, such as beam-beam effects. However, if the transverse emittances decrease much more rapidly than protons are consumed at the collision points, the beam-beam tune shift may exceed the beam-beam limit, or the bunch length may become so short that the beam loses longitudinal Landau damping. Fortunately, this is not expected to be the case for the nominal LHC parameters with continually colliding beams, since the synchrotron-radiation damping is still moderate, and, in addition, it will partially be balanced by intra-beam scattering [49]. The expected evolution of key beam parameters and luminosity during a 10-h physics store is displayed in Fig. 5.3. If necessary, the balance of intra-beam scattering and synchrotron radiation can be modified by a judicious blow up of the longitudinal emittance using noise excitation.

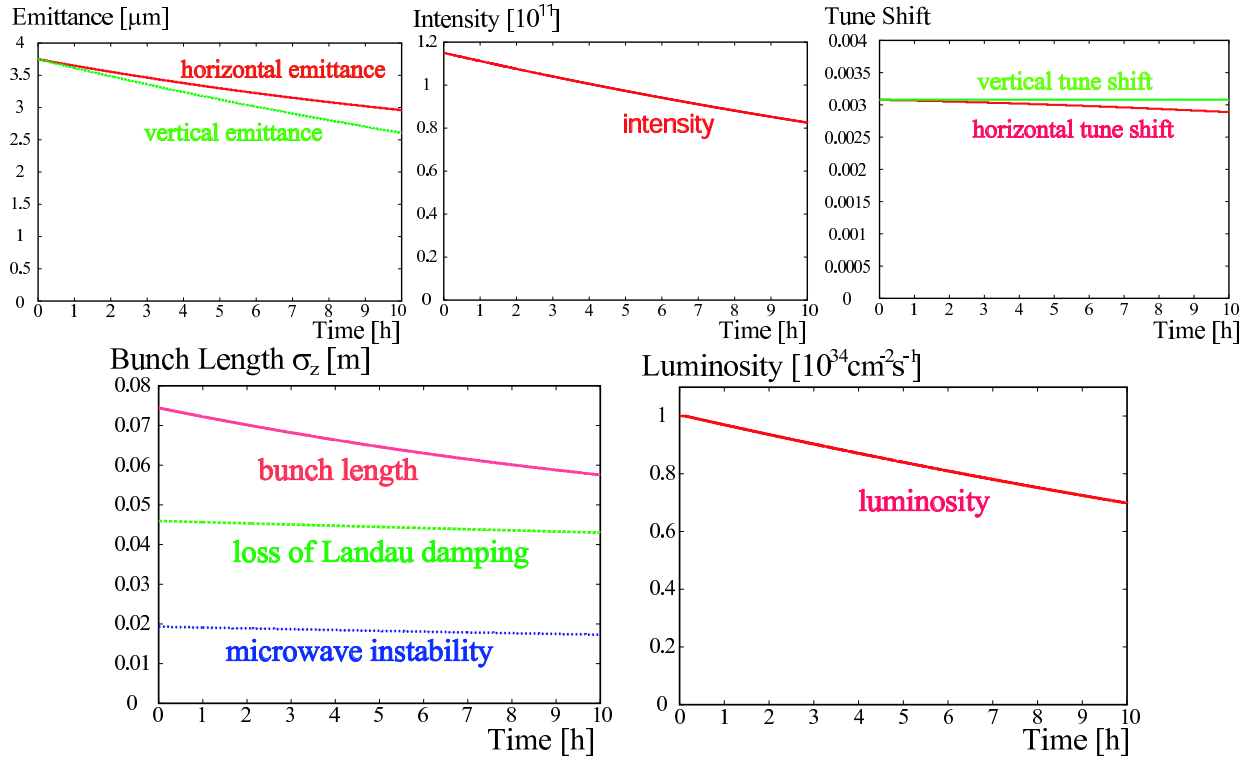

Figure 5.3: Evolution of normalized emittances (top left), bunch intensity (top centre), head-on beam-beam tune shift at the two high-luminosity IP's (top right), rms bunch length together with estimated limits for the loss of Landau damping and the onset of the longitudinal microwave instability (bottom left), and luminosity (bottom right) as a function of time during a nominal physics store at 7 TeV. The effect of intra-beam scattering (evaluated according to the approximate formulae in [50] and assuming a 10% vertical growth rate due to betatron coupling or vertical dispersion, corresponding to initial longitudinal/horizontal/vertical emittance growth times of 68/98/983 h), particle consumption at the two high-luminosity IP's (with a total inelastic cross section of 100 mbarn), and synchrotron radiation (with longitudinal/horizontal emittance damping times of 13/26 h) is included. The effect of residual gas scattering (with $\tau_{\mathrm{nucl}} \geq 100$ h) and other possible mechanisms leading to emittance growth, such as electron cloud, RF noise, ground motion, tune modulation or amplitude diffusion induced by the beam-beam interaction, is not included.

5.7 HEAT LOAD SUMMARY

A summary of the heat load induced on the arc beam screen by the nominal LHC beam at injection and at 7 TeV is shown in Tab. 5.7. The heat load caused by the electron cloud depends on the secondary electron yield of the beam screen surface and is discussed in Sec. 5.8.3.

Detailed estimates of the heat deposition by the nuclear scattering of the protons colliding in each of the two high luminosity LHC experiments can be found in [51]. These dynamic heat loads scale with the machine luminosity and, for nominal LHC luminosity of $10^{34}\,\mathrm{cm}^{-2}\,\mathrm{s}^{-1}$, they range between 5 and 13 W/m in the IR regions. In particular the power deposition in the inner triplet amounts to 30.7 W, 28.8 W, 26.6 W, and 27.7 W for the quadrupoles Q1, Q2a, Q2b, and Q3, respectively.

Table 5.7: Summary of heat load on the arc beam screen for nominal LHC beam at 7 TeV. The three columns give the source, the latest relevant reference, and the peak heat load in mW/m.

source	Ref.	Peak power [mW/m] at 7 TeV
Synchrotron Radiation	[48]	220
Ohmic Losses	[52]	110
Pumping Slots	[53]	10
Welds	[2]	10

5.8 ELECTRON CLOUD EFFECTS

A significant number of electrons can accumulate in the LHC beam pipe, due to the close bunch spacing of 25 ns [10]. This *electron cloud* could largely increase the heat load deposited on the LHC arc beam screen [11, 12]. It may also degrade the vacuum pressure, as observed, for example, in the ISR [54] and more recently in the SPS [55] and in RHIC [56], induce single- or multi-bunch instabilities [57, 58, 59, 60], and possibly cause long-term emittance growth. Electron clouds are presently limiting the performance of several operating storage rings, notably the two B factories, PEP-II and KEKB [61], the Los Alamos Proton Storage Ring [62], and RHIC [56]. An electron cloud occurs with LHC-type beam in the CERN SPS, where many of its characteristics, including heat load and conditioning effects, can be studied in situ for conditions resembling those of the LHC [55]. Primary electrons — the seed of the electron cloud — are created by a variety of different processes. The number of electrons then increases exponentially by a process known as *beam-induced multipacting*, in which the electron amplification is the result of secondary emission from the chamber wall.

In the LHC design, a number of countermeasures are incorporated, which aim either at suppressing an electron-cloud build-up or at alleviating its effect. These measures include (1) a sawtooth chamber in the arcs, which reduces the photon reflectivity, (2) shielding the pumping holes inside the arc beam screen so as to prevent multipacting electrons from reaching the cold bore of the dipole magnets, (3) coating the warm regions by a special getter material, TiZrV, with low secondary emission yield, and (4) conditioning of the arc chamber surface by the cloud itself (*beam scrubbing*), which will ultimately provide a low secondary emission yield. During commissioning the bunch spacing can be increased and/or the beam energy be reduced to process the chamber while staying within the available cooling capacity.

5.8.1 Photoelectrons and Secondary Emission

An electron cloud builds up, if a modest number of primary electrons is amplified during the passage of a bunch train. This amplification occurs due to acceleration of electrons in the field of the beam and subsequent secondary emission with an average yield larger than one.

At injection energy, primary electrons are mainly generated by gas ionization or beam loss. At top energy, the primary electron flux is strongly enhanced, due to photoemission from synchrotron radiation. This latter process does not contribute to the electron seed at injection, since here the photon energies are too low to generate any photoelectrons. The number of photons emitted per radian is given by $5/(2\sqrt{3})\,\gamma/137$, which, at 7 TeV, is about 79 photons per proton and per radian deflection angle. For an LHC half cell of 53.45 m length and 15.3 mrad bending angle, this amounts to 0.023 photons incident per proton and per metre at 7 TeV. On the LHC Cu sawtooth chamber and with the LHC photon spectrum, the initial probability of photoemission is 5%, decreasing to about 2.5% after conditioning [63]. The primary synchrotron radiation at 7 TeV is incident on the outer wall of the chamber according to a Gaussian vertical distribution of about 1.4 mm rms in height. The

azimuthal distribution of the absorbed photons determines the region from where photo-electrons are emitted. In a dipole magnet, photo-electrons can reach the vicinity of the beam only if they come from the top or bottom of the chamber. Thus it is desirable to absorb the maximum number of photons at their primary impact point on the horizontally outward side of the beam pipe, and to keep the photon reflection as low as possible. One distinguishes forward, diffuse, and backward reflection. In the LHC a low forward reflectivity is accomplished by impressing a sawtooth surface on the beam screen (*i.e.*, the inner part of the beam pipe). However, about 20% of the incident photons are diffusely reflected from the sawtooth, roughly according to a $\cos^2\phi$ distribution (where ϕ denotes the angle of the reflected photon with respect to the horizontal plane), so that about 10% of the reflected photons (or 2% of the total) may be absorbed at the top and bottom of the chamber [64]. Preliminary experimental data on photon backward reflection indicate that this effect would only yield a small additional contribution [65]. In simulations, the measured energy distribution of the emitted photoelectrons [66] is approximated by a (one-sided truncated) Gaussian with a peak at 3 eV and an rms spread of 3 eV. The photoelectron emission angles are assumed to be distributed uniformly in spherical coordinates.

Secondary electron emission consists of two components: the true secondaries and the elastically reflected electrons. The true secondary yield as a function of the primary impact energy E_p is expressed by the Furman formula [67] $\delta_{\rm true}(E_p) = \delta_{\rm max} s E_p/E_{\rm max}/(s-1+(E_p/E_{\rm max})^s)$, where $s \approx 1.35$ and the two parameters $\delta_{\rm max}$ and $E_{\rm max}$ describe the maximum yield and the energy at which it is attained. These parameters vary with the angle of incidence. Laboratory measurements indicate that $E_{\rm max}(\theta) \approx E^0_{\rm max}(1+0.7\,(1-\cos\theta))$ [67] and $\delta_{\rm max}(\theta) \approx \delta^0_{\rm max}\exp(0.5\,(1-\cos\theta))$ [68], where quantities with superscript 0 refer to perpendicular incidence. The values of $\delta^0_{\rm max}$ and $E^0_{\rm max}$ characterize the degree of conditioning. In the laboratory, samples are fully conditioned after depositing an electron dose of 10 mC/mm^2 [69], and values of $\delta^0_{\rm max}$ below 1.3 can be obtained after a dose of 2 mC/mm^2 [69]. The final conditioning effect may depend not only on the total dose, but also on the electron flux during the processing [70]. Fully conditioned laboratory samples at room temperature sometimes exhibit maximum secondary emission yields as low as $\delta^0_{\rm max} \approx 1.1$. Similar yields after conditioning were also observed at cryogenic temperatures [71]. In-situ measurements with room-temperature detectors at the SPS in 2002 and 2003 showed $\delta^0_{\rm max} \approx 2.35$ and $E^0_{\rm max} \approx 260$ eV for the initial state, and $\delta^0_{\rm max} \approx 1.5$ and $E^0_{\rm max} \approx 240$ eV after about 2 days of dedicated 'beam scrubbing' [72]. Following this initial decrease, $\delta^0_{\rm max}$ remained approximately constant for several days until the end of the scrubbing period. This saturation at $\delta^0_{\rm max} \approx 1.5$ in the SPS is attributed to operational constraints on the available beam intensities and to the re-adsorption of the residual gas [70]. First preliminary measurements with cold detectors in the SPS suggest that the scrubbing time at cryogenic temperatures might be longer than at room temperature [73, 74]. For LHC simulation purposes, the value of $E^0_{\rm max}$ corresponding to a certain value of $\delta^0_{\rm max}$ has been estimated by linear interpolation from the above numbers for the SPS (see Tab. 5.8). The energy distribution of the true secondaries is concentrated at low energies, and can be parametrized as in [69], namely $D(E_s) \propto \exp(-(\ln E_s/E_0)^2/2\tau^2)$, where $E_0 \approx 1.8$ eV and $\tau \approx 1$ are two fitting parameters. For this distribution, the average emission energy of the true secondaries is $\bar{E}_s \approx 8.1$ eV. The initial angular distribution of the true secondaries in spherical coordinates, $dN/d\Omega$, is taken to be of the form $\cos\theta$, where θ denotes the emission angle of the secondary electron with respect to the surface normal [75].

For incident electrons of low energy, a significant portion of the secondary electrons are not true secondaries, but instead they are elastically reflected electrons. Depending on the interpretation of the experimental low-energy data, the yield of elastic reflection can be expressed in two different ways: First, one may write the elastic yield as $\delta_{\rm el} = f/(1-f)\delta^0_{\rm true}$, where f is the measured ratio of elastic reflections to the total number of secondaries, which may be parametrized as in [69]. Second, an alternative parametrization is derived from the assumption that the electron reflectivity is not affected by the conditioning process, and that it always approaches the value of 1 in the limit of zero primary energy. This assumption can be modelled by the parametrization $\delta_{\rm el} = (\sqrt{E_p+E_0}-\sqrt{E_p})^2/(\sqrt{E_p+E_0}+\sqrt{E_p})^2$. The single parameter $E_0 \approx 150$ eV has been fitted from measurements [76]. This second parametrization gives rise to a minimum in the total secondary yield, at around 10 eV, which appears consistent with many of the experimental data, *e.g.*, in [76], but it could still prove an artifact of the measurement apparatus. Fig. 5.4 displays alternative curves for the total secondary emission yield at perpendicular incidence, $SEY \equiv \delta_{\rm true}+\delta_{\rm el}$, as a function of the primary electron energy, corresponding to the different parametrizations. The centre curve assumes the first model of elastic

reflection, the top curve the second. For completeness, the bottom curve shows the Furman's formula for true secondaries only, using the parameters $\delta^0_{\max} = 1.06$ and $E^0_{\max} = 262\,\text{eV}$ ($\delta_{\text{el}} = 0$). Most simulations in this report have been performed for the first model (centre curve), which includes a moderate amount of elastic electron reflection. It is always assumed that, unlike for the true secondaries, the yield of the elastic reflection, δ_{el}, is independent of the angle of incidence.

Table 5.8: Typical LHC simulation parameters related to electron cloud build-up at 7 TeV.

parameter	initial	final
maximum secondary emission yield $\delta^0_{\max}$	1.9	1.1
energy for which yield is maximum, $\epsilon^0_{\max}$	249 eV	230 eV
photo-electrons per absorbed photon	5%	2.5%
photo-electrons per proton and metre in the arc	0.00116	0.00058
photon reflectivity R	20%	20%
parameter for elastic electron reflection E_0	150 eV	150 eV

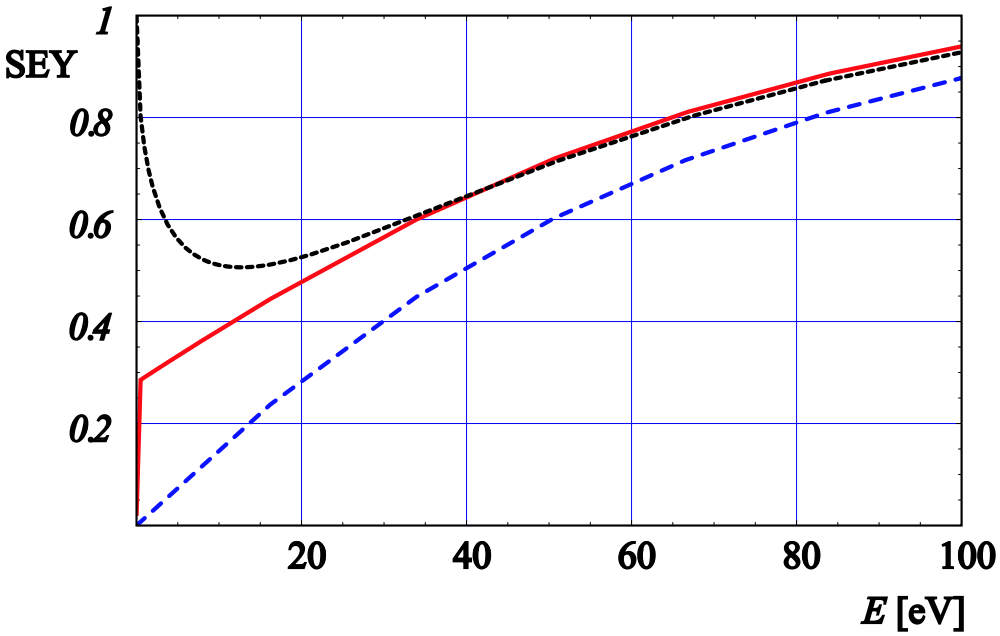

Figure 5.4: Model of the total secondary emission yield, $SEY = \delta_{\text{true}} + \delta_{\text{el}}$, at perpendicular incidence, as a function of the primary electron energy, assuming no elastic reflection (long dashes, bottom curve), a secondary emission that decreases at low energies towards about 0.3 (solid, centre curve), and the model that seems to best fit the measured data in [76], with a minimum near 10 eV and a reflection probability of one for incident energies approaching zero (short dashes, top curve). The other parameters for this graph correspond to the laboratory measurement of a fully scrubbed Cu surface at 9 K ($\delta^0_{\max} = 1.06$, $E_{\max} = 262\,\text{eV}$) [76].

5.8.2 Build-Up and Saturation

If an electron amplification occurs, the cloud builds up until the growth is balanced by its own space charge. This limit can arise either if the average charge of the electrons equals that of the protons (neutralization) [10] or when, in the time interval between two proton bunches, the space charge potential exceeds the initial kinetic energy of the secondaries [77]. Thus, the estimated saturation density is the smaller value of [10, 77] $\rho_e^{(1)} \approx \bar{E}_s/(m_e c^2 b^2 r_e)$ and $\rho_e^{(2)} \approx N_b/(\pi b^2 L_{\text{sep}})$, where L_{sep} denotes the bunch spacing in metres. For the nominal LHC parameters, these limiting densities are quite comparable: $\rho_e^{(1)} \approx 1.4 \times 10^{13}\,\text{m}^{-3}$ and $\rho_e^{(2)} \approx 1.2 \times 10^{13}\,\text{m}^{-3}$. As an illustration, Fig. 5.5 presents some simulations for the electron cloud build-up in the LHC

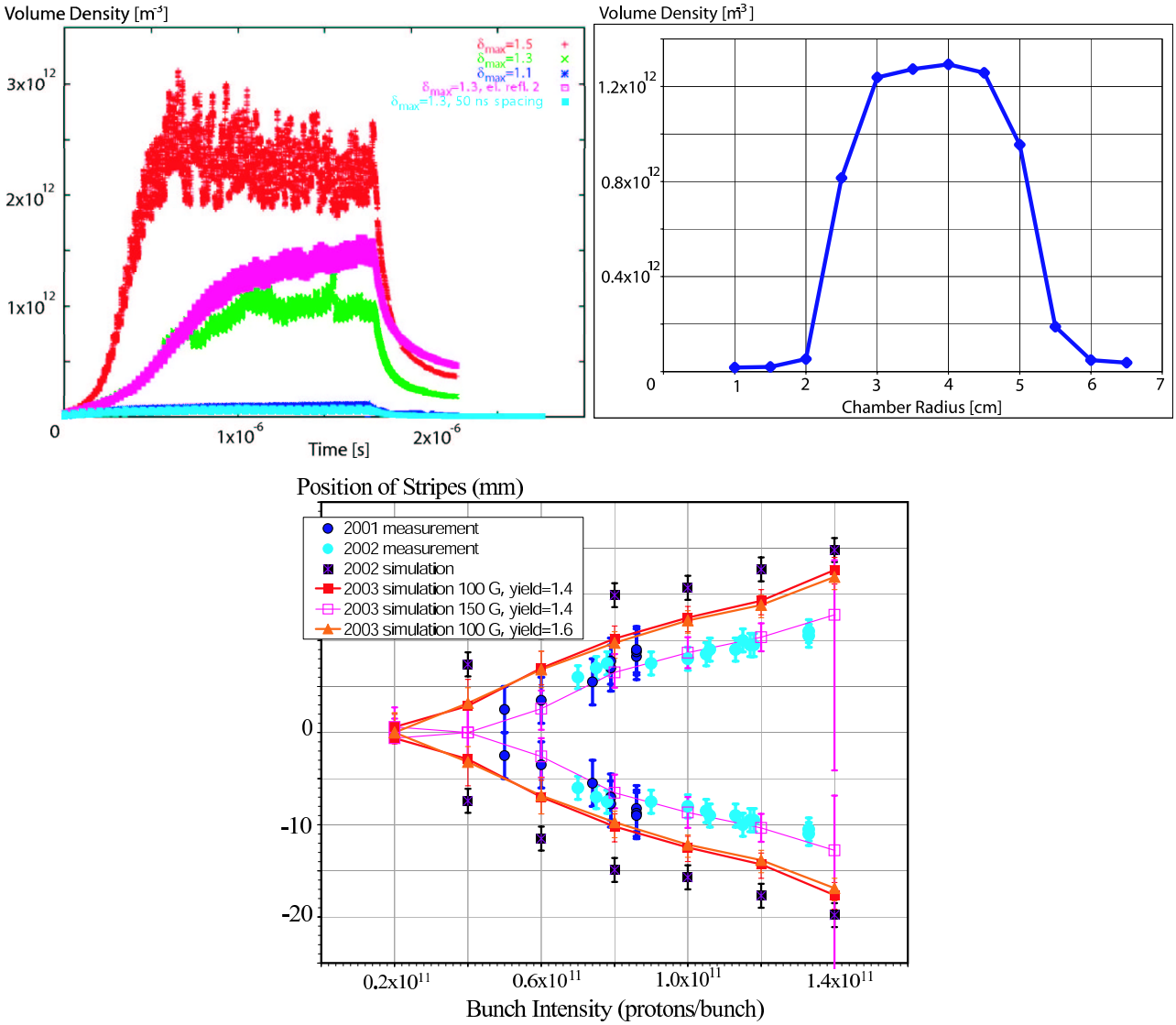

Figure 5.5: Top left: simulated electron volume density [m^{-3}] in an arc dipole as a function of time [s], for $N_b = 10^{11}$, various values of $\delta_{\max}$, two bunch spacings, and two models of the elastic electron reflection; top right: the simulated electron density [m^{-3}] in a circular field-free region of the long straight section as a function of beam pipe radius [cm], for $N_b = 1.15 \times 10^{11}$ and $\delta^0_{\max} = 1.3$; bottom: the horizontal position of regions with high electron multipacting ("stripes") measured inside a dipole magnetic field at the SPS during 2001 and 2002 [55], as a function of bunch intensity, compared with simulations performed in 2002 and 2003. The effects of altering the magnetic field and using different values of $\delta^0_{\max}$ are also shown [12].

and in the SPS, which were obtained using ECLOUD version 2.5. The top left picture shows the simulated build-up of electron density during the passage of an LHC bunch train (a single PS batch) through an arc cell for a bunch population of $N_b = 10^{11}$. The various curves refer to different values of $\delta^0_{\max}$, to the two models of elastic reflection, and to two different bunch spacings. For the range of $\delta^0_{\max}$ values considered here, the steady-state densities are determined by a balance of production and decay rates, and stay at least a factor of 10 below the ultimate space-charge saturation limit estimated above. The top right picture of Fig. 5.5 displays the simulated steady-state electron volume density as a function of aperture, for a field-free region, assuming $N_b = 1.15 \times 10^{11}$, and $\delta_{\max} = 1.3$. The primary photo-electron flux in this simulation was taken to be 20 times smaller than in the arcs, which is representative of the long straight sections. The picture illustrates that for a single beam, radial apertures between 25 and 55 mm are most susceptible to an electron-cloud build-up. Similar simulations have been performed for the SPS, where a reasonable agreement between various

simulated and measured electron-cloud properties, such as spatial structure, flux, energy spectrum, and heat load, was achieved [12, 55]. An example is shown in the bottom picture of Fig. 5.5, which illustrates the horizontal position of two narrow regions with high multipacting ("stripes"), as measured and simulated for an SPS dipole field. Since the vertical chamber dimension in the SPS is nearly the same as that for an LHC dipole, the location of the stripes is also expected to be similar in both accelerators, and, therefore, the observed and predicted variation of the stripe location with intensity in the SPS has motivated the addition of baffles at each LHC-beam screen pumping slot, which block the passage of electrons onto the cold bore of the magnets.

5.8.3 Heat Load

The heat load deposited by the electron cloud is a concern for the cold parts of the LHC, where it may quench the super-conducting magnets. Inside the 1.9-K cold bore of the magnets, the electron-cloud heat load is intercepted by a dedicated beam screen, which is held at a higher temperature of 5–20 K. As mentioned in Sec. 5.8.2, pumping holes in the beam screen are shielded by baffles, such that the electron cloud does not contribute to the heat load onto the 1.9-K cold bore. The heat load for the latter is then dominated by nuclear interactions, depositing about 0.035 W/m [43], which is to be compared with a cooling capacity of 0.32 W/m per beam at 1.9 K [78]. The total available cooling capacity for the warmer beam screen is 1.15 W/m per beam [78]. In addition to the heat from the electron cloud, this number must also accommodate the heat loads due to synchrotron radiation and impedance. The synchrotron-radiation heat load increases linearly with the total beam current, while the impedance contribution rises quadratically with the bunch population N_b. For the ultimate LHC intensity of $N_b = 1.67 \times 10^{11}$, the average arc heat load due to synchrotron radiation is 0.25 W/m, and that from impedance (res. wall, welds, pumping slots, shielded bellows, and BPMs) is estimated at 0.41 W/m [79]. The remaining cooling capacity, about 0.5 W/m at nominal intensity and energy, may be allocated to the electron cloud. The expected average electron-cloud heat loads in the arcs for various surface and beam conditions are computed by averaging simulation results over a 53.452-m long arc half cell, which comprises a field-free region of length 6.433 m, a dipole field of 42.9 m, and quadrupole plus sextupole fields extending over a length of 4.119 m.

Fig. 5.6 displays simulation results, obtained with ECLOUD version 2.5, for the steady-state electron density and the heat load generated during the passage of an LHC bunch train. The three pictures show the heat load and the electron volume density as a function of bunch population and also as a function of each other. The various curves refer to three different values of $\delta^0_{\max}$, to the two models of elastic electron reflection, and to both the nominal and twice the nominal bunch spacing. The available cooling capacity is also indicated, in the top left picture. For the nominal bunch spacing a maximum secondary emission yield of $\delta^0_{\max} = 1.1$ ensures sufficient cooling capacity, while for larger values of $\delta^0_{\max}$, *e.g.*, 1.3, doubling the bunch spacing reduces the heat load to an acceptable level. On the other hand, bunch spacings shorter than nominal likely increase the heat load to unacceptable values, so that enlarging the number of bunches does not appear a viable path towards ultimate LHC luminosities in a future upgrade [45]. Colliding a smaller number of long super-bunches, instead, would promise both a high luminosity and a much reduced electron-cloud heat load [80], but imply substantial detector upgrades.

5.8.4 Beam Stability

At various storage rings, for example the SPS, electron clouds have caused beam instabilites and disrupted operation. In the SPS a coupled-bunch instability is observed in the horizontal plane, and a single bunch instability in the vertical [59, 60]. The strengths of the electron-cloud single-bunch and multi-bunch wake fields ($W_{\rm sb}$ and $W_{\rm mb}$) are estimated as [58, 81] $W_{\rm sb} \approx 2W_{\rm mb} \approx 8\pi\rho_e C/N_b$, where C denotes the circumference, ρ_e the average electron density, N_b the bunch population, and the wakes are quoted in units of m^{-2}. The corresponding growth rate of the coupled-bunch instability is [81] $\tau_{e,\rm CB} \approx \gamma/(2\pi r_p c\bar{\beta}\rho_e)$, and the threshold of the single-bunch ('TMCI'-like) instability can be expressed as a threshold in the electron density as [58] $\rho_{e,\rm thr} \approx 2\gamma Q_s/(\pi\bar{\beta}r_p C)$, where Q_s denotes the synchrotron tune, and $\bar{\beta}$ the average beta function.

The instabilities are primarily a concern at injection, where the beam is less rigid. Here, the estimated multi-bunch instability rise times vary between 2 and 2000 turns, depending on the electron density. The effect

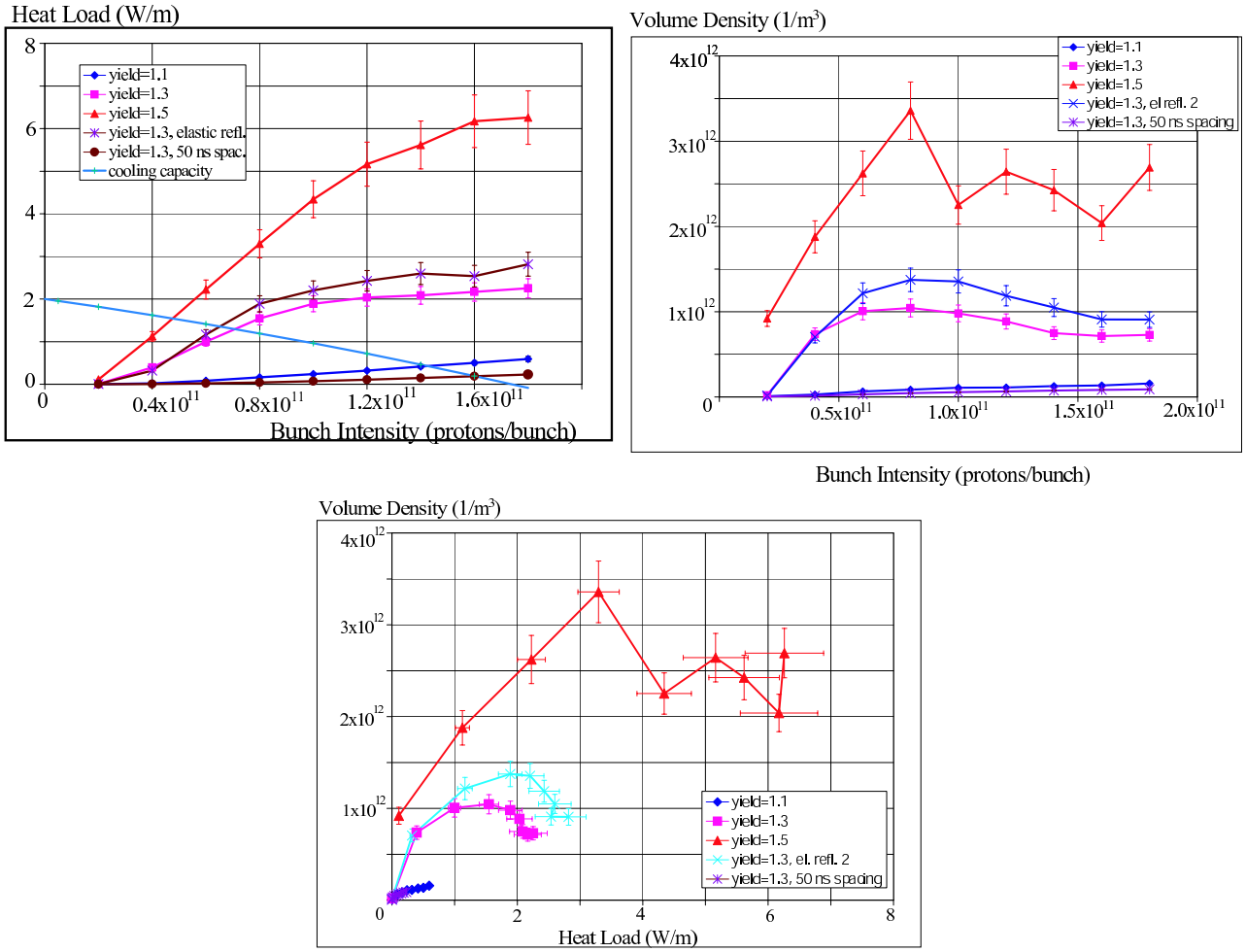

Figure 5.6: Simulated electron-cloud heat load and density for the LHC: average arc heat load and available beam screen cooling capacity (assuming an upgrade of the turbines for the four LEP cryoplants) as a function of bunch population (top left), simulated average electron volume density in the arc for the last bunch in a train as a function of the bunch population (top right), and simulated volume density as a function of simulated heat load for an LHC arc cell (bottom). Results for three different values of $\delta^0_{\max}$ (1.1, 1.3 and 1.5), using the first model of elastic reflection, are compared with those for the second model and for twice the nominal bunch spacing, at the intermediate value $\delta^0_{\max} = 1.3$.

of the electron cloud can be enhanced by the conventional impedance [82, 83], and also by the beam-beam interaction [84, 85]. Simulation studies of single-bunch instabilities driven by the electron cloud, with and without impedance, were performed using the code HEADTAIL for both the LHC and the SPS [82, 86]. For zero chromaticity, the simulations indicate an instability threshold at about $\rho_e \approx 5 \times 10^{11}$ m^{-3}. Above the threshold, the single-bunch emittance growth time decreases roughly inversely with the electron density. It is 160 turns for an average electron cloud density of $\rho_e \approx 10^{12}\,\mathrm{m}^{-3}$, and only 16 turns for $\rho_e \approx 10^{13}\,\mathrm{m}^{-3}$. Hence, if strong multipacting occurs in the arcs of the LHC, the strength of the vertical single-bunch instability may become comparable to that in the SPS. Both in the SPS experiments and in the simulations, the emittance growth is suppressed by a high positive chromaticity. This could also prove a viable cure for the LHC.

The actual magnitude of the electron density can be inferred from the induced coherent tune shift as [87] $\Delta Q \approx r_p \bar{\beta} \rho_e C/(2\gamma)$. For full saturation of the electron density ($\rho_e \approx 1.2 \times 10^{13}\,\mathrm{m}^{-3}$) the expected tune shift amounts to 0.05. As shown in Fig. 5.6, for $\delta^0_{\max} = 1.5$ a maximum electron density $\rho_e \approx 3 \times 10^{12}\,\mathrm{m}^{-3}$ is expected and therefore a maximum tune shift at the end of a bunch train of about 0.015. The measured tune shifts in the SPS are of the order of 0.01.

5.8.5 Emittance Growth

Simulations indicate the possibility that the electron cloud may sustain long-term emittance growth [86]. The simulated emittance growth sensitively depends on the details of the simulation model, however, such as whether the beam-electron interaction is applied at random betatron phases or at the same constant phase from turn to turn. For the former case the growth seems to converge towards zero, as the number of beam-electron interaction points is increased in the code HEADTAIL [82, 86]. Nevertheless it is not excluded, that an incoherent emittance growth may occur due the incoherent tune spread induced by the pinched electrons or due to nonlinear resonances, *e.g.*, of order 3–10, which can be excited by the electron cloud [86]. This question can be investigated by QUICKPIC [88] simulations, which model the continuous interaction of the beam and the electrons.

5.8.6 Electron Cloud at Collimators

An electron cloud could also be generated at the collimators. In this case, the primary source of electrons are not photoelectrons, but electrons emerging from the nuclear and electromagnetic shower initiated by lost protons. In preliminary FLUKA simulations [89], 7-TeV protons impinged on a graphite collimator jaw with impact parameters uniformly distributed between 0 and 200 nm from the collimator edge. From the simulation, the fluence spectrum (*i.e.*, the flux weighted by $1/\cos\theta$) of charged hadrons, electrons and positrons emitted from the jaw was obtained, down to energies of 1 keV. Assuming a factor of 5 mg/(MeV cm^2) for the conversion efficiency of ionization energy into secondary electrons at perpendicular incidence [90], a beam lifetime of about 15 minutes yields an estimated total flux of low-energetic electrons emerging from a primary collimator jaw equal to 1.3×10^{14} s^{-1} [89], or, equivalently, 4×10^{-5} electrons per passing proton. This rate is comparable to the photoemission in the LHC arcs. More detailed studies of the lower-energy secondary electrons generated by the collimator shower and their longitudinal distribution may be needed. Assuming a maximum secondary emission yield $\delta_{\max} = 1.1$, the saturation level of the electron cloud density is about 2.5×10^{10} m^{-3}, *i.e.*, somewhat smaller than typical arc densities. The dependence on the collimator half-gap is weak.

5.8.7 LHC Strategy

The LHC design has adopted a fourfold strategy for suppressing the formation of an electron cloud:

(1) In the warm sections, which amount to about 10% of the total circumference, the beam pipe will be coated by a TiZrV getter developed at CERN [91]. This getter does not only provide an excellent pumping performance, but after activation, at only 180°C, its maximum secondary emission yield drops down to $\delta^0_{\max} \approx 1.1$ [92, 93, 94], a value for which a significant electron cloud build-up is no longer expected. The non-existence of an electron cloud in getter-coated regions has been confirmed in SPS experiments [95]. Even in the unlikely event that an electron-cloud builds up in the warm sections of the LHC, the getter still has its virtue. Namely, ionization of gas molecules by the low-energy electrons, with a high cross section of up to 400 Mbarn, and the subsequent absorption of the ionized molecules by the getter significantly increases the pumping speed in the affected regions. Therefore, different from past storage rings, the pressure in the LHC experimental areas is expected to improve, if a cloud develops.

(2) In the arcs, the outer wall of the beam screen, at 5–20 K, will be equipped with a sawtooth surface (a series of 30-μm high steps spaced at a distance of 500 μm in the longitudinal direction) such that the synchrotron radiation always impinges perpendicularly on the sawtooth surface. The sawtooth greatly reduces the forward reflectivity from about 80% to 2%. The largest residual reflectivity is a diffuse reflection of about 20%. A low reflectivity of the outer chamber wall is desired, since in bending magnets photoelectrons emitted from this outer region are confined by the strong dipole field and do not interact much with the beam (see also Sec. 5.8.1).

(3) The pumping slots in the beam screen are shielded by baffles, so that, in the dipoles, there is no direct electron path along magnetic field lines between the beam region and the cold bore, and, therefore, also no additional heat load onto the latter (see Secs. 5.8.2 and 5.8.3).

(4) Operating the LHC with nominal parameters relies on the surface conditioning (scrubbing) effect, akin to the processing of an RF cavity, by which the maximum secondary emission yield decreases from an initial

value of about 2 to about 1.4 or below, after depositing a sufficient dose of electrons on the chamber wall (see discussion in Sec. 5.8.1). During commissioning, when the yield is still high, an increased bunch spacing and/or a reduced bunch intensity will greatly reduce the heat load. However this will also slow down the scrubbing of the vacuum chamber.

5.9 BEAM-BEAM EFFECTS

An important limit to the luminosity comes from the beam-beam effect which can cause emittance increase, poor lifetime or instabilities. Different types of beam-beam effects can be distinguished and affect the performance in different ways:

- Incoherent beam-beam effects (lifetime and dynamic aperture).
- PACMAN effects (bunch-to-bunch variations).
- Coherent effects (beam oscillations and instabilities).

5.9.1 Relevant parameters

The high luminosity requires a large number of bunches (2808) and to avoid unwanted collisions, a crossing angle is needed to separate the two beams in the part of the machine where they share a vacuum chamber. The size of the crossing angle is limited by the available aperture in the final quadrupole triplet and for high luminosity operation a crossing angle of 285 μrad is planned. For $\beta^* = 0.55$ m this provides a separation $\mathrm{d_{sep}}$ above $9\,\sigma$. With the bunch spacing of 25 ns this leads to a total of 120 long-range beam-beam interactions in the four interaction regions. Both the head-on and the long-range interactions have to be considered when beam-beam effects are studied. The strength of head-on collisions is usually measured by the linear beam-beam parameter ξ which for small values and nominal betatron tunes is equivalent to the linear tune shift of small amplitude particles. It can be written as $\xi = N_{\mathrm{b}} r_{\mathrm{p}}/4\pi\varepsilon_{\mathrm{n}}$ where N_{b} is the number of particles per bunch, r_{p} the classical proton radius and ε_{n} the normalized emittance. With nominal parameters we get a value of 0.0033 for a single head-on collision in the LHC.

5.9.2 Incoherent effects

When the beam passes through the strong non-linear field of the opposing beam, the dynamics of single particles can be strongly distorted up to the point where they are lost from the beam. Different factors are shown which are used to quantify this behaviour. The experience obtained at the Tevatron and the SPS proton antiproton collider is very relevant although basic parameters such as the number of bunches and the importance of long-range collisions are very different.

Beam-beam induced tune spread: budget from past experience (SPS and Tevatron)

Due to its non-linear nature, the beam-beam interaction will lead to an amplitude dependent tune spread in both planes. This spread must be accommodated in the tune diagram without crossing dangerous resonance lines. Thus the total spread originating from head-on and long range beam-beam interactions is very important and must be kept as small as possible [96, 97]. Experience from the SPS and the Tevatron shows that the total tune spread including all other sources and the beam-beam effect, should not exceed 0.015 [98]. This allows about ≈0.01 for the overall beam-beam tune spread ΔQ_{bb}. The tune spread from a head-on collision, ΔQ_{ho}, is ξ, which is the maximum tune shift. For sufficiently large separation, i.e. above $6\,\sigma$, the tune spread from long-range interactions, ΔQ_{lr}, is approximately proportional to $\frac{\kappa_{\mathrm{par}} N_{\mathrm{b}}}{\varepsilon_{\mathrm{n}}}/d_{\mathrm{sep}}^2$. Here κ_{par} is the total number of long range (parasitic) interactions. As an example Fig. 5.7 shows the tune distribution (footprint) for the nominal proton parameters with three head-on collisions, one offset collision (IP2) and the full number of long-range interactions. Particles up to amplitudes of $6\,\sigma$ are included. The overall spread is slightly above 0.010 in agreement with the requirements.

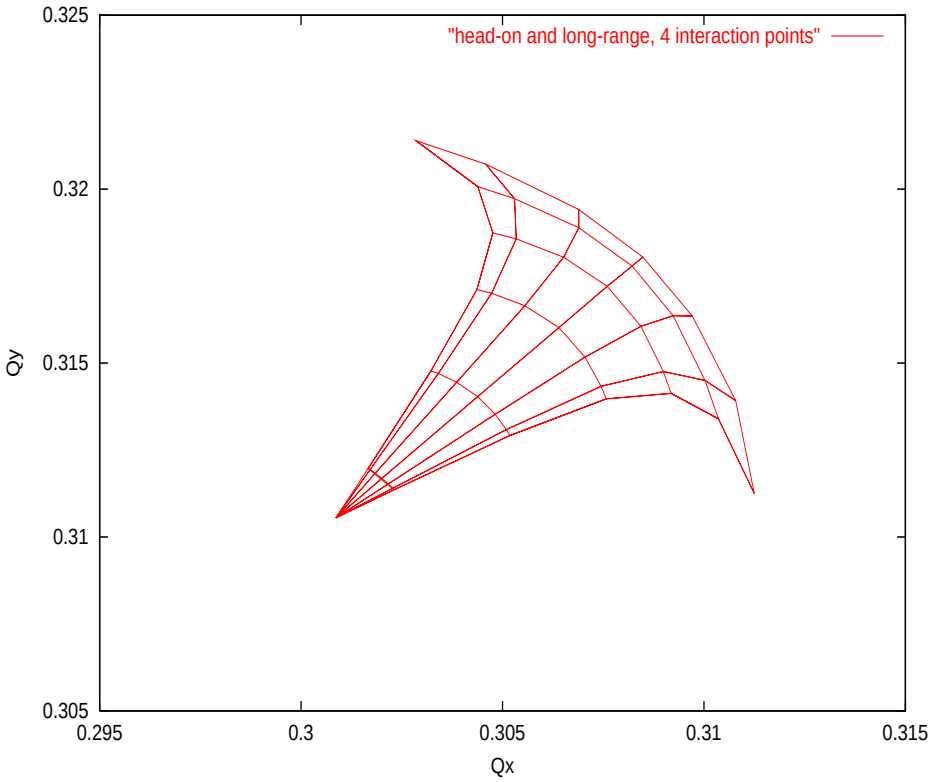

Figure 5.7: Two dimensional tune distribution versus amplitude (footprint) for nominal parameters in collision. Particles up to amplitudes of 6 σ are included.

Emittance variations from bunch-to-bunch will have implications for both long range and head-on beam-beam effects. In the first case they will reduce the normalized beam separation and therefore the available dynamic aperture for bunches with larger emittances. In the second case, head-on collisions of bunches with unequal sizes are known to lead to particle losses for the bunches with larger sizes [99]. Bunch-to-bunch emittance variations should therefore not exceed about 10%.

Dynamic aperture

An important single particle effect of the head-on and especially of the long range beam-beam interaction is the reduction of the beam lifetime due to the diffusion of large amplitude particles towards the aperture limit [100, 101]. The effects of the triplet errors together with the beam-beam interaction was intensively studied for collision as well as for injection [100]. In both cases the beam-beam interaction leads to a sizeable reduction of the dynamic aperture. Fig. 5.8 shows the results for 10^5 and 10^6 turns when the beam-beam interaction at collision is included. It was found that even very small non-linearities are sufficient to lead to particle losses when the beam-beam force is present. Therefore, the benefits of the triplet correction system are much reduced, in particular when longer term tracking is performed. Fig. 5.9 shows the results at injection. For comparison the dynamic aperture without beam-beam interaction is shown. The reduction of the aperture is very significant, in particular for a large number of turns. A more detailed discussion of the results can be found in [100]. Some approximate scaling [101] suggests that the reduction of dynamic aperture is proportional to $\sqrt{\frac{\kappa_{\mathrm{par}} N_{\mathrm{b}}}{\varepsilon_{\mathrm{n}}}}$, i.e. $\propto \sqrt{\Delta Q_{\mathrm{lr}}}$, which shows the relevance of the tune spread.

5.9.3 PACMAN effects

The bunches in the LHC do not form a continuous train of equidistant bunches spaced by 25 ns, but additional space must be provided to allow for the rise time of kickers. The whole LHC bunch pattern is composed of

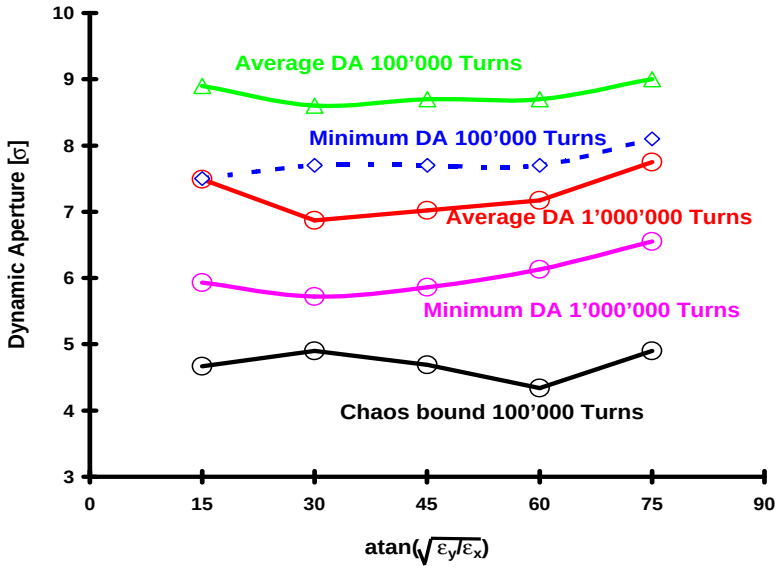

Figure 5.8: Dynamic aperture at collision including beam-beam interaction. Tracking is performed for 10^5 and 10^6 turns.

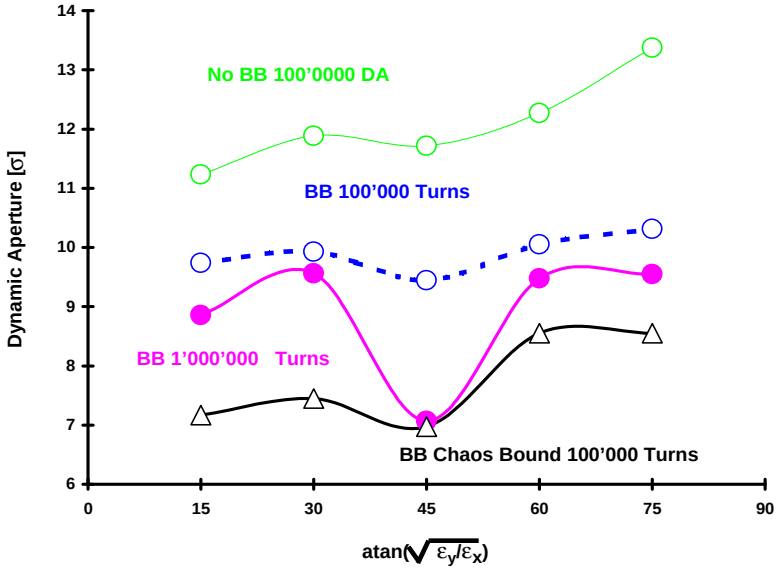

Figure 5.9: Dynamic aperture at injection with and without beam-beam interaction. Tracking is performed for 10^5 and 10^6 turns.

39 smaller trains of 72 bunches separated by gaps of various lengths (Fig. 5.10) including a large abort gap for the dump kicker. Due to the symmetric layout, all bunches collide head-on in interaction points 1 and 5. However, bunches at the beginning and end of a train suffer only half the long-range interactions at each interaction point [102]. As a consequence, they experience only half the accumulated beam-beam effects and may have a different dynamics [102]. The actual bunch filling scheme is presented in Fig. 5.10 and shows the various gaps in the train. Since the pattern does not have a complete fourfold symmetry, certain bunches will encounter the abort gap in points 2 and 8, therefore missing head-on collisions. A further complication is introduced by LHCb in interaction point 8 because the collision point is displaced by 11.22 m (corresponding to 15 RF buckets or 37.5 ns) from the symmetry point. Therefore the first three bunches of each train in one beam and the last three bunches of the other beam do not collide head-on in interaction point 8. As a consequence a significant number of bunches experience three (252 bunches) or only two (3 bunches) out of the four head-on collisions. Instead of 2808 bunch crossings per revolution as in interaction points 1 and 5, only 2736 will happen in interaction point 2 and only 2622 in 8. Bunches which do not have the regular collision pattern

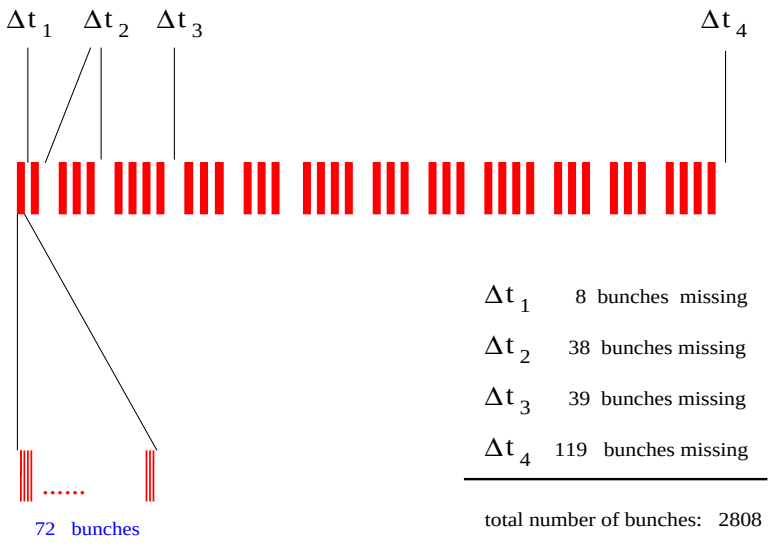

Figure 5.10: Bunch filling scheme for the LHC.

have been named PACMAN bunches in the literature. Only 1443 bunches are regular bunches with 4 head-on and 120 long range interactions, i.e. about half of the bunches are not regular. The identification of regular bunches is important since measurements such as tune, orbit or chromaticity should be selectively performed on them.

Bunch-to-bunch variation

As a result of the different accumulated beam-beam effects, a bunch-to-bunch variation of vital parameters such as orbit, tune and chromaticity must be expected. Such variations have been observed in LEP and have limited the performance [98]. While tune or orbit changes of the whole beam can be corrected, this is not possible on a bunch-to-bunch basis. It is therefore important to minimize these effects. A particular feature of long-range interactions helps in this case. The derivatives of the transverse force for head-on and long-range interactions have different signs and therefore the tune shift has a different sign in the plane of separation with respect to the orthogonal plane. This feature can be used for a partial compensation of beam-beam effects and becomes vital to minimize bunch-to-bunch variations. All calculations of bunch-to-bunch variations are done for nominal parameters, in particular for the nominal bunch intensity of 1.15×10^{11} particles per bunch.

Crossing schemes

It was already mentioned in the chapter on the optics that the crossings in the high luminosity regions (interaction points 1 and 5) occur in orthogonal planes [103, 104]. Since these regions are exactly opposite in azimuth, the same bunch combinations will experience long-range and head on interactions in the two regions, although in different planes. Having horizontal, respectively vertical, long-range interactions for the same bunch combinations can efficiently compensate their effects to first order. In particular the tune shifts of the bunches are compensated. To allow a good compensation, the two interaction regions should have a similar layout. The two other interaction regions in points 2 and 8 have a larger β^* and do not significantly contribute to long-range interactions. Therefore no compensation is required. More details and an evaluation of the stability of the compensation in the presence of imperfections are discussed in [105].

Orbit effects

The beam-beam kick for separated beams has a constant, i.e. amplitude independent contribution which changes the orbit of a bunch. The closed orbit of a beam can be corrected, however different orbits from bunch-to-bunch, separated by 25 ns, cannot be corrected. In general, these patterns are not antisymmetric for the two

beams and not all bunches can be made to collide head-on [102]. A small offset is therefore unavoidable which could lead to emittance growth [106]. One has to minimize these effects by a proper choice of the crossing schemes [105] and the filling pattern [107]. The compensation effect on the orbit of individual bunches is

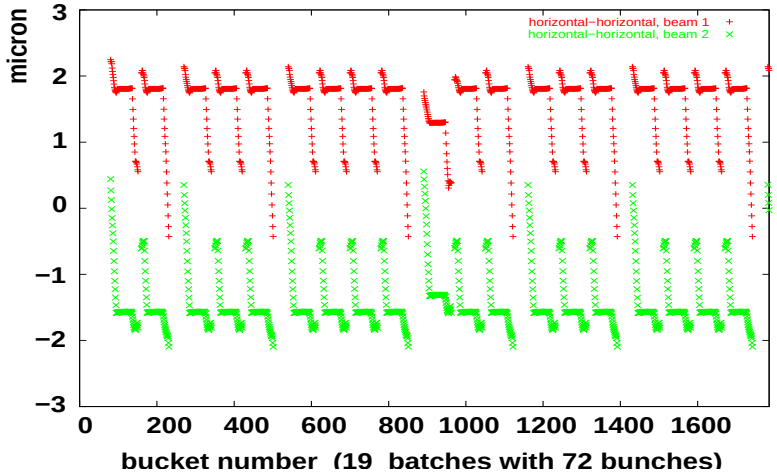

Figure 5.11: Horizontal orbit variation for beam 1 (upper trace) and beam 2 (lower trace) at interaction point 1 for horizontal-horizontal crossing. The first half of the whole bunch pattern is shown.

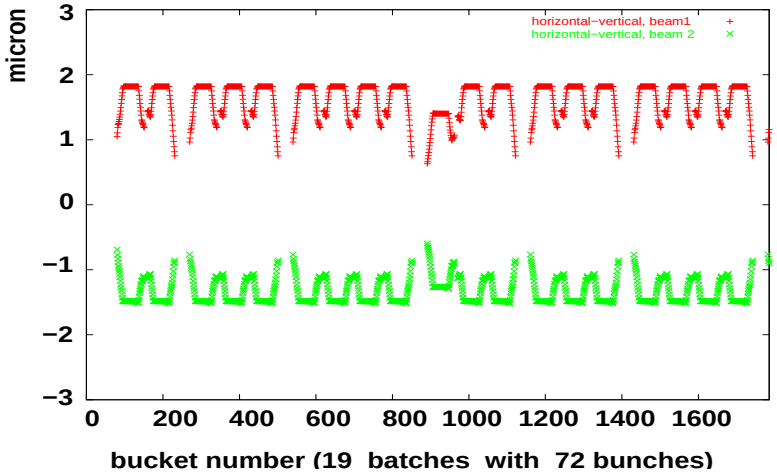

Figure 5.12: Horizontal orbit variation for beam 1 (upper trace) and beam 2 (lower trace) at interaction point 1 for vertical-horizontal crossing. The first half of the whole bunch pattern is shown.

demonstrated in Figs. 5.11 and 5.12. In both the calculated horizontal offset of the bunches along the bunch trains in interaction point 1 are shown. The calculation is done self-consistently using the full collision scheme and the beam optics of both beams [108]. The bunches are affected as a whole and the coherent beam-beam kick is calculated and applied. The first figure shows the closed orbits of the two beams for two horizontal crossings in interaction points 1 and 5 and the second for alternating, i.e. vertical (IP1) and horizontal (IP5) crossings [105]. The crossing planes in IP2 (vertical) and IP8 (horizontal) are the nominal for both cases. The beams in IP2 are separated to reduce the luminosity in proton-proton collisions. The different orbits of the leading and trailing bunches are very visible. The regular bunches all have the same closed orbit and appear on a straight line in the central part of the bunch trains. The orbit spread within the bunch train is significantly smaller in the second case. While in the first case the maximum orbit spread within the trains is approximately 2.5 μm, it is only around 0.9 μm for the case of alternating crossing planes. Only half of the whole bunch pattern is shown since no significant information is added for the full bunch pattern. The effect of the large abort gap is visible for the bunches with bucket numbers around 860. Due to the symmetry of the crossing schemes, the vertical offsets in interaction point 5 show the same behaviour [105]. The vertical orbits in IP1

and the horizontal orbits in IP5 are antisymmetric due to the symmetry properties and the beams can collide head-on, although not in the centre of the collision point [105]. Since these effects are intensity dependent, the orbits may move and partially separate the beams at the interaction point during a typical LHC run when the intensity decays. A further source of beam separation is very low frequency ground motion. It was shown [109] that a separation of about 0.5 σ has to be expected during a typical 8 hours run. Both effects have to be corrected during an LHC run to maintain the maximum integrated luminosity.

Tune and chromaticity

In Figs. 5.13 and 5.14 results from the self-consistent calculation [108] for the horizontal tune (Fig. 5.13) and the horizontal chromaticity (Fig. 5.14) are shown. While all regular bunches have practically the same tune and chromaticity, the PACMAN bunches show significant differences. For the case of two horizontal crossings the spread is probably too large to ensure a safe operation. Similar results can be obtained for the vertical plane [105]. The compensation is very good and clearly demonstrates the necessity for the alternating crossing planes. The missing head-on collisions result in a different coherent tune of the bunches and the structure is very visible, showing the missing collisions of the first three bunches in each batch and the position of the abort gap. Additional spread is expected from unavoidable bunch to bunch fluctuations of the intensity and emittance. To keep the spread acceptable, the variation of both, intensity and emittance should not be larger than 10% [105]. It is therefore vital to minimize the systematic variations induced by beam-beam effects. For bunch intensities higher that the nominal, the alternating scheme is even more a necessity [110].

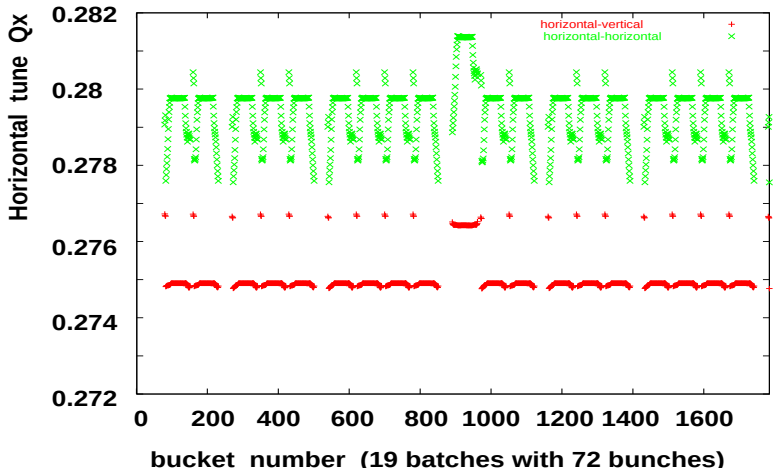

Figure 5.13: Horizontal tune variation along the first half of the batches. Horizontal-horizontal crossing in green (upper trace), vertical-horizontal crossing in red (lower trace).

5.9.4 Coherent effects

The LHC will be a machine with two equally strong beams and coherent beam-beam effects may be expected [111, 112]. Coherent modes of oscillations of the two counter rotating beams are coupled by the beam-beam interaction. They may become unstable depending on the strength of the beam-beam interaction and the other machine parameters. The most dangerous mode is the coherent dipole mode where a bunch oscillates as a rigid object around its nominal orbit. The predictions can be confirmed by multi-particle tracking [113]. The frequency spectrum of these coherent dipole oscillations is shown in Fig. 5.15 (left). The frequencies are shown as a tune change with reference to the unperturbed tune, normalized with the linear beam-beam tune shift. Fig. 5.15 (left) was produced with a multi-particle simulation using a recently developed algorithm for the field calculation [114] which gives quantitatively correct results. Only a single interaction point with one head-on interaction is considered to demonstrate the main features. The presence of long-range interactions complicates the picture and the underlying physics, but does not change the argument [114, 115]. All frequencies are contained in an interval limited by two discrete mode, the so-called σ- and π-modes. For the σ-mode

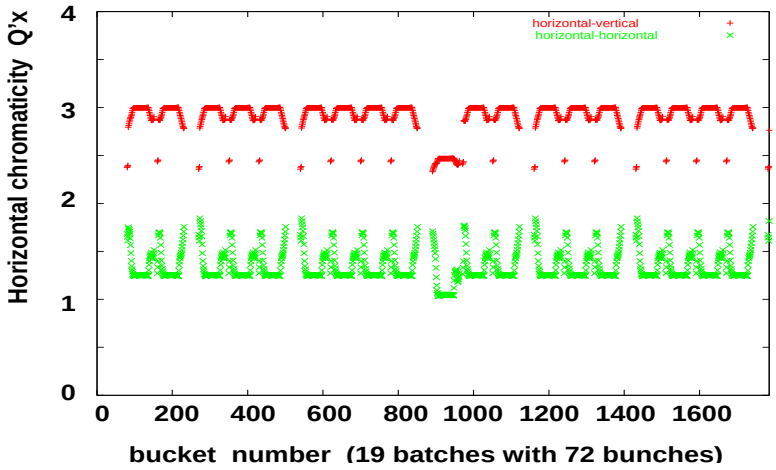

Figure 5.14: Horizontal chromaticity variation along the first half of the batches. Horizontal-horizontal crossing in green (lower trace), vertical-horizontal crossing in red (upper trace).

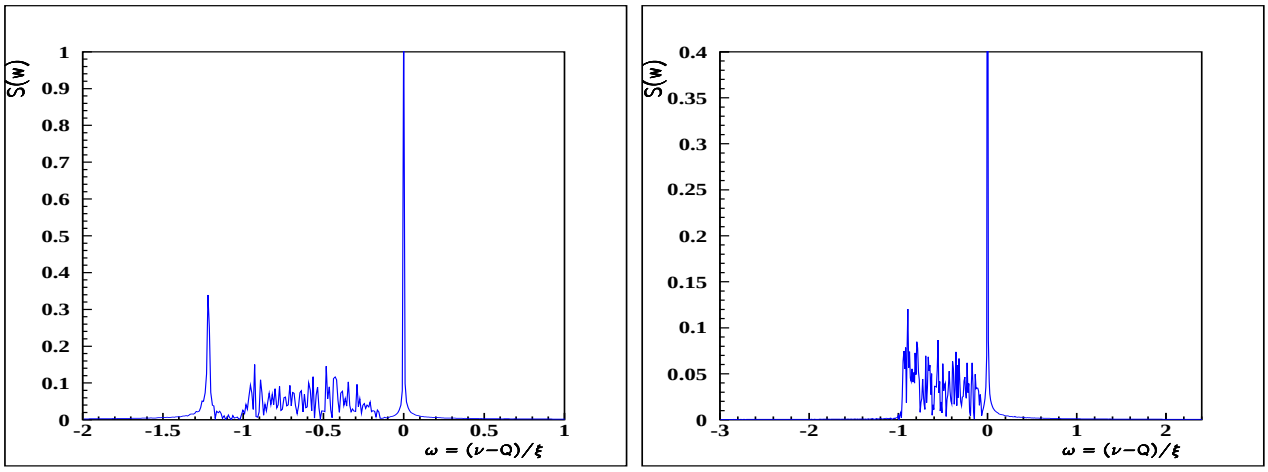

Figure 5.15: Frequency spectrum of dipole oscillation. One interaction point with a single bunch. Left figure shows spectrum for two identical beams. Right figure for an intensity ratio of 0.55 between the two beams.

the two beams oscillate exactly in phase, i.e. the distance between the two beams is constant when they collide and the beam-beam force cannot make this mode unstable. Furthermore, this mode oscillates with the unperturbed betatron frequency. In the π-mode the two beams oscillate exactly out of phase and this mode can become unstable and has the largest frequency shift with respect to the unperturbed tune. The tune shift of the π-mode is approximately $1.21\,\xi$ for round beams [111] (Fig. 5.15 left). Y. Alexahin predicted [112, 116] that for the nominal LHC parameters the π-mode will be outside the incoherent frequency spectrum which is due to beam-beam effects and extends from 0 to ξ for a single interaction region. This is reproduced by the simulation and clearly shown in Fig. 5.15 (left). Therefore the discrete π-mode will be outside this incoherent continuum and cannot be stabilized by Landau damping. The Landau damping can be restored when the symmetry between the two beams is broken [115], e.g. by different intensities (Fig. 5.15, right), different tunes [117], or broken symmetry for multiple interaction regions [118]. The frequency spectrum for two unequal beams with an intensity ratio of 0.55 is shown in 5.15 (right). The π-mode is now inside the continuum and is damped. This is quantitatively predicted in [112]. Additional degrees of freedom such a longitudinal motion and the overlap with synchrotron sidebands have been shown to effectively suppress the coherent π-mode [119]. It is believed that the symmetry breaking effects present in the LHC (multiple IPs, the already mentioned bunch-to-bunch fluctuations etc.) are sufficient to suppress the excitation of coherent modes driven by the beam-beam interaction.

REFERENCES

[1] The LHC Study Group, *Design Study of the Large Hadron Collider (LHC)*, CERN report 91-03 (1991).

[2] F. Ruggiero, *Single-beam collective effects in the LHC*, CERN SL/95-09 (AP), LHC note 313 (1995) and Proc. Workshop on 'Collective Effects in Large Hadron Colliders', Montreux, 1994, eds. E. Keil and F. Ruggiero (Part. Accel. **50**, 1995), pp. 83–104, see also LHC Study Group, *The Large Hadron Collider, Conceptual Design*, eds. P. Lefevre and T. Pettersson, CERN/AC/95-05 (LHC) (1995).

[3] J.S. Berg, *Transverse instabilities in the LHC*, CERN LHC Project Report 16 (1996) and *Constraints imposed on LHC commissioning currents due to transverse collective modes and chromaticity*, CERN LHC Project Report 100 (1997).

[4] F. Ruggiero, J.S. Berg, O. Brüning, F. Caspers, M. Morvillo, and M. D'Yachkov, *Summary of the Single-Beam Collective Effects in the LHC*, PAC 97, Vancouver and CERN LHC Project Report 120 (1997).

[5] D. Boussard, D. Brandt, and L. Vos, *Is a longitudinal feedback system required for LHC?*, CERN LHC Project Note 205 (1999).

[6] D. Brandt and L. Vos, *Resistive wall instability for the LHC: intermediate review*, CERN LHC Project Note 257 (2001).

[7] E. Shaposhnikova, *Longitudinal phenomena during the LHC cycle*, Proc. Chamonix 2001, CERN-SL-2001-003 DI (2001).

[8] D. Angal, D. Brandt, and L. Vos, *Intermediate review of single bunch collective effects in the LHC*, EPAC 2002 and CERN LHC Project Report 587 (2002).

[9] D. Angal, *Review of Coupled Bunch Instabilities in the LHC* , CERN LHC Project Report 595 (2002), see also D. Angal, and L. Vos, *Coupled bunch instabilities in the LHC*, EPAC 2002 and CERN LHC Project Report 585 (2002).

[10] F. Zimmermann, *A Simulation Study of Electron-Cloud Instability and Beam-Induced Multipacting in the LHC*, CERN LHC Project Report 95 (1997).

[11] O. Gröbner, *Beam Induced Multipacting*, PAC 97, Vancouver, and CERN LHC Project Report 127 (1997), J.S. Berg, *Energy Gain in an Electron Cloud During the Passage of a Bunch*, CERN LHC Project Note 97 (1997), G. Stupakov, *Photoelectrons and Multipacting in the LHC: Electron Cloud Build-up*, CERN LHC Project Report 141 (1997), O. Brüning, *Simulations for the Beam-Induced Electron Cloud in the LHC beam screen with Magnetic Field and Image Charges*, CERN LHC Project Report 158 (1997), F. Caspers, J.-M. Laurent, M. Morvillo, and F. Ruggiero, *Multipacting tests with a resonant coaxial setup*, CERN LHC Project Note 110 (1997), F. Ruggiero, *Electron Cloud in the LHC*, CERN LHC Project Report 166 (1998), M. Furman, *The Electron Cloud Effect in the Arcs of the LHC*, CERN LHC Project Report 180 (1998), L. Vos, *Electron Cloud: an Analytic View*, CERN LHC Project Note 150 (1998), V. Baglin et al., *Beam-Induced Electron Cloud in the LHC and Possible Remedies*, EPAC 1998, Stockholm, and CERN LHC Project Report 188 (1998), F. Zimmermann, *Electron Cloud Simulations: An Update*, Proc. Chamonix 2001, CERN-SL-2001-003 DI (2001). See also World-wide web page on *Electron Cloud in the LHC* at the address `http://wwwslap.cern.ch/collective/electron-cloud/`.

[12] F. Zimmermann, *Electron Clouds – Operational Limitations and Simulations*, Proc. Chamonix 2003, CERN-AB-2003-008 ADM (2003).

[13] J.-P. Koutchouk, *Correction of the long-range beam-beam effect in LHC using electro-magnetic lenses*, CERN SL-2001-048-BI (2001) and Proc. IEEE Particle Accelerator Conference (PAC2001), Chicago, IL, USA, 18–22 June 2001, eds. P. Lucas and S. Webber (IEEE, Piscataway, NJ, 2001), pp. 1681–1683.

[14] F. Ruggiero and F. Zimmermann, *Luminosity optimization near the beam-beam limit by increasing bunch length or crossing angle*, CERN SL-2002-005-AP (2002) and Phys. Rev. ST Accel. Beams **5**, 061001 (2002).

[15] K. Yokoya, *Resistive wall impedance of beam pipes of general cross section*, KEK report 92-196 (1993).

[16] L. Vos, *The transverse impedance of a cylindrical pipe with arbitrary surface impedance*, CERN-AB-2003-005-ABP (2003).

[17] H. Tsutsui, *Resistive wall impedance of an LHC collimator*, CERN LHC Project Note 318 (2003).

[18] L. Vos, *The impedance of multi-layer vacuum chambers*, CERN-AB-2003-093-ABP (2003).

[19] S. Calatroni, et al., *Design aspects of the RF contacts for the LHC beam vacuum interconnects*, CERN LHC Project Report 491 (2001).

[20] M. Gyr, *Expected magnetic field quality of the LHC septum magnets used for injection (MSI) and for extraction to the beam dump (MSD)*, CERN LHC Project Note 129 (1998).

[21] F. Caspers and A. Mostacci, *Bench Measurements of the LHC Injection Kicker Low Frequency Impedance Properties*, CERN SL-Note-2002-030 AP (2002), see also L. Ducimetiere, et al., *Design of the injection kicker magnet system for CERN's 14 TeV proton collider LHC*, CERN SL-95-80 BT (1995).

[22] R. Gluckstern, L. Vos, and B. Zotter, *Shielding particle beams by thin conductors*, CERN SL-2002-014 AP (2002).

[23] R. Gluckstern, *Coupling Impedance of Many Holes in a Liner within a Beam Pipe*, CERN SL/92-06 (AP) (1992).

[24] D. Brandt, B. Spataro, and L. Vos, *Impedance of the LHC arc beam position monitors*, CERN LHC Project Note 284 (2002); L. Vos and A. Wagner, *Longitudinal impedance of LHC version-1 stripline beam position monitor*, CERN LHC Project Report 126 (1997).

[25] D. Brandt, et al., *Impedance of the LHC recombination chambers*, CERN LHC Project Note 254 (2001). See also D. Brandt et al., *On trapped modes in the LHC recombination chambers: numerical and experimental results*, CERN LHC Project Report 604 (2002) and L. Vos, *Considerations about the impedance of the Y-chamber*, SL-AP Beam Physics Note 50 (2000), `http://slap.web.cern.ch/slap/beam_physics.html`.

[26] M. D'Yachkov, *Impedance of the rough LHC beam pipe*, SL-AP Beam Physics Note 8 (1998), see `http://slap.web.cern.ch/slap/beam_physics.html`.

[27] J. Gareyte, *Impedances: Measurements and Calculations for Non-symmetric Structures*, EPAC 2002, Paris, and CERN SL-2002-028 (2002).

[28] A.W. Chao, *Physics of Collective Beam Instabilities in High Energy Accelerators*, (Wiley, New York, 1993).

[29] E. Metral, *Collective effects in the CERN-PS beam for LHC*, Proc. Workshop on 'Instabilities of high intensity hadron beams in rings', Upton, NY (AIP Conf. Proc. **460**, 1999), p. 116. There seems to be some disagreement in the community about the role of space charge impedance and tune spread in transverse instabilities, see same Proc. p. 398. Preliminary results on the combined treatment of direct space charge and lattice nonlinearities, to appear in a forthcoming report by E. Metral et al., indicate that the stability diagram is dominated by the space charge tune spread for negative real tune shifts and by the lattice nonlinearities for positive real tune shifts and imaginary tune shifts.

[30] K. Bane and P.L. Morton, *Deflection by the Image Currentand Charges of a Beam scraper*, Proc. 1986 Linac Accelerator Conference, Stanford, CA, SLAC-PUB-3983 (1986).

[31] F. Zimmermann, K. Bane, and C. Ng, *Collimator Wake Fields in the SLC Final Focus*, EPAC 1996, Sitges, Barcelona, SLAC-PUB-7137 (1996).

[32] K. Yokoya, *Impedance of Slowly Tapered Structures*, CERN SL/90-88 (AP) (1990).

[33] G. Stupakov, *Geometrical Wake of a Smooth Taper*, SLAC-PUB-95-7086 (1995).

[34] O. Brüning, *ZBASE User's Guide Version 1.1 : an Impedance Data Base Program*, CERN-SL-96-069 AP (1996).

[35] L. Vos, *Transverse Emittance Blow-up from Dipole Errors in Proton Machines*, EPAC 1998, Stockholm, and CERN LHC Project Report 193 (1998).

[36] J.S. Berg and F. Ruggiero, *Landau Damping with two-dimensional betatron tune spread*, CERN SL-96-71 AP (1996).

[37] J. Gareyte, J.-P. Koutchouk, and F. Ruggiero, *Landau Damping, Dynamic Aperture and Octupoles in LHC*, CERN LHC Project Report 91 (revised version, 1997); J.-P. Koutchouk and F. Ruggiero, *A Summary on Landau Octupoles for the LHC*, CERN LHC Project Note 163 (1998).

[38] W. Herr and L. Vos, *Tune distributions and effective tune spread from beam-beam interactions and the consequences for Landau damping in the LHC*, CERN LHC Project Note 316 (2003).

[39] O. Brüning and S. Fartoukh, *Field Quality Specification for the LHC Main Dipole Magnets*, CERN LHC Project Report 501 (2001), p. 7.

[40] H. Grote and F.C. Iselin, *The MAD Program, User's Reference Manual*, CERN SL/90-13 (AP) (Rev. 4) (1995), see also J. Bjorken and S. Mtingwa, Part. Acc. **13**, 115 (1983).

[41] F. Ruggiero, *Parameters for First Physics and for* 10^{33}, Proc. Chamonix 2003, CERN AB-2003-008 ADM (2003).

[42] F. Zimmermann and M.-P. Zorzano, *Touschek Scattering in HERA and LHC*, CERN LHC Project Note 244 (2000).

[43] O. Gröbner, *The LHC Vacuum System*, in CERN Accelerator School on 'Vacuum Technology for Particle Accelerators', Snekersten, Denmark, CERN Yellow Report CERN-99-05 (1999), pp. 291–306.

[44] The Particle Data Group, *Review of Particle Physics*, Eur. Phys. J. C**3**, 1–794 (1998).

[45] O. Brüning, et al., *LHC Luminosity and Energy Upgrade: A Feasibility Study*, edited by F. Ruggiero, CERN LHC Project Report 626 (2003).

[46] G. Stupakov, *Geometrical Wake of a Smooth Flat Collimator*, SLAC-PUB-7167 (1996).

[47] G. Stupakov, *High-Frequency Impedance of Small-Angle Collimators* and P. Tenenbaum et al., *Transverse Wakefields from Tapered Collimators: Measurements and Analysis*, PAC 2001, Chicago (2001).

[48] F. Zimmermann, *Synchrotron Radiation in the LHC Arcs — Monte-Carlo Approach*, CERN LHC Project Note 237 (2000); A. Rossi and F. Zimmermann, *Synchrotron Radiation in the LHC Experimental Insertions*, CERN LHC Project Report 675 (2003).

[49] F. Zimmermann, *Luminosity Limitations at Hadron Colliders*, Proc. 18th Conf. High Energy Accelerators (HEACC 2001), Tsukuba, and also CERN-SL-2001-009-AP (2001).

[50] K.L.F. Bane, *A Simplified Model of IntraBeam Scattering*, Proc. EPAC 2002, Paris, p. 1443 (2002).

[51] N. Mokhov, et al., *Protecting LHC IP1/IP5 Components Against Radiation Resulting from Colliding Beam Interactions*, CERN LHC Project Report 633 (2003).

[52] F. Caspers, M. Morvillo, F. Ruggiero, J. Tan, and H. Tsutsui, *Surface Resistance Measurements of LHC Dipole Beam Screen Samples*, EPAC 2000, Stokholm, and CERN LHC Project Report 410 (2000).

[53] A. Mostacci and F. Ruggiero, *Pumping slots and thickness of the LHC beam screen*, CERN LHC Project Note 195 (1999).

[54] O. Gröbner, *Bunch Induced Multipacting*, 10th Int. Conference on High Energy Accelerators, Protvino (1977).

[55] J.M. Jimenez et al., *Electron Cloud with LHC-Type Beams in the SPS: A Review of Three Years of Measurements*, CERN LHC Project Report 632 (2003).

[56] S.Y. Zhang et al., *RHIC Pressure Rise and Electron Cloud*, PAC 2003, Portland (2003).

[57] K. Ohmi, *Beam and Photoelectron Interactions in Positron Storage Rings*, Phys. Rev. Letters **75**, 1526 (1995).

[58] K. Ohmi and F. Zimmermann, *Head-Tail Instability Caused by Electron Cloud in Positron Storage Rings*, Phys. Rev. Letters **85**, 3821–3824 (2000).

[59] K. Cornelis, *The Electron Cloud Instability in the SPS*, Proc. ECLOUD'02, Geneva, 15–18 April, 2002, CERN Yellow Report CERN-2002-001 (2002).

[60] G. Arduini et al., *The Electron Cloud Instability of the LHC Beam in the CERN SPS*, PAC 2003, Portland, and CERN LHC Project Report 637 (2003).

[61] H. Fukuma, *Electron Cloud Effects at KEKB*, Proc. ECLOUD'02, Geneva 15–18 April, CERN Yellow Report CERN-2002-001 (2002).

[62] D. Neuffer et al., *Observations of a Fast Transverse Instablity in the PSR*, NIM A**321**, 1 (1992), and R. Macek, *Studies of the Electron Cloud at the LANL PSR*, Int. Workshop on Two-Stream Instabilities, Tsukuba, September 11–14 (2001).

[63] V. Baglin, I.R. Collins, O. Grobner, C. Grunhagel, B. Henrist, N. Hilleret, B. Jenninger, "Measurements at EPA of Vacuum and Electron-Cloud Related Effects," Proc. Chamonix 2001, CERN-SL-2001-003 DI, p. 141 (2001).

[64] I.R. Collins, private communication (2000), see also V.V. Anashin et al., *Magnetic and Electric Field Effects on the Photoelectron Emission from Prototype LHC Beam Screen Material*, CERN LHC Project Report 373 (1999).

[65] N. Mahne, V. Baglin, I.R. Collins, A. Giglia, L. Pasquali, M. Pedio, S. Nannarone, and R. Cimino, *Photon Reflectivity Distributions from the LHC Beam Screen and Their Implications on the Arc Beam Vacuum System*, 8th European Vacuum Conference, Berlin, and LHC Project Report 668 (2003).

[66] R. Cimino, I.R. Collins, and V. Baglin, *VUV Photoemission Studies of Candidate Large Hadron Collider Vacuum Chamber Materials*, Phys. Rev. ST Accel. Beams **2**, 063201 (1999).

[67] M. Furman and G. Lambertson, *The Electron-Cloud Instability in the Arcs of the PEP-II Positron Ring*, Proc. Int. Workshop on Multibunch Instabilities in Future Electron and Positron Accelerators (MBI 97), Tsukuba, KEK, KEK Proceedings 97-17 (1997).

[68] R. Kirby and F. King, *Secondary Electron Emission from Accelerator Materials*, 8th ICFA Beam Dynamics Mini-Workshop on 'Two-Stream Instabilities', SLAC-PUB-8380 (2000).

[69] V. Baglin, et al., *A Summary of the Main Experimental Results Concerning the Secondary Electron Emission of Copper*, CERN LHC Project Report 472 (2002).

[70] N. Hilleret, *SEY Measurements During the Scrubbing Run*, minutes of the CERN Accelerator Performance Committee meeting of 01.08.2003, `http://ab-div.web.cern.ch/ab-div/Meetings/APC/`.

[71] R. Cimino, I.R. Collins, *Vacuum Chamber Surface Electronic Properties Influencing Electron Cloud Phenomena*, 8th European Vacuum Conference, Berlin, and LHC Project Report 669 (2003).

[72] N. Hilleret, private communication (2003) and *SEY and Pick-up Calorimeter Measurements*, Mini-Workshop on 'SPS Scrubbing Run Results and Implications for the LHC', CERN, 28 June 2002, `http://sl.web.cern.ch/SL/sli/Scrubbing-2002/Workshop.htm`.

[73] J.M. Jimenez, *Vacuum Effects During the SPS Scrubbing Run*, minutes of the CERN Accelerator Performance Committee meeting of 01.08.2003, `http://ab-div.web.cern.ch/ab-div/Meetings/APC/`.

[74] V. Baglin, *Preliminary Results from COLDEX*, minutes of the CERN Accelerator Performance Committee meeting of 01.08.2003, `http://ab-div.web.cern.ch/ab-div/Meetings/APC/`.

[75] H. Seiler, *Secondary Electron Emission in the Scanning Electron Microscope*, J. Appl. Phys. **54**, 11 (1983).

[76] R. Cimino et al., *Can Low Energy Electrons Affect High Energy Physics Accelerators?*, CERN-AB-2004-012-ABP (2004).

[77] S. Heifets, *Electron Cloud at High Beam Currents*, Proc. ECLOUD'02, Geneva, 15–18 April, 2002, CERN Yellow Report CERN-2002-001 (2002).

[78] P. Lebrun, *Large Cryogenic Helium Refrigeration System for the LHC*, CERN LHC Project Report 629 (2003).

[79] Web site of the LHC heat load working group, `http://lhc-mgt-hlwg.web.cern.ch/`.

[80] F. Ruggiero, G. Rumolo, F. Zimmermann, Y. Papaphilippou, *Beam dynamics studies for uniform (hollow) bunches or super-bunches in the LHC: beam–beam effects, electron cloud, longitudinal dynamics, and intra-beam scattering*, RPIA2002 Workshop, KEK, Tsukuba, and CERN LHC Project Report 627 (2002).

[81] G. Rumolo and F. Zimmermann, *Two-Stream Problems in Accelerators*, Proc. 2nd APAC Conference, Beijing, 2001, and CERN-SL-2001-057-AP (2001).

[82] G. Rumolo and F. Zimmermann, *Electron-Cloud Simulations: Beam Instabilities and Wake Fields*, Proc. ECLOUD'02, CERN, Geneva, 15–18 April, 2002, CERN Yellow Report CERN-2002-001 and Phys. Rev. ST Accel. Beams **5**, 121002 (2002).

[83] K. Cornelis, *Interplay between SPS Impedance and Electron Cloud*, Mini-Workshop on 'SPS Scrubbing Run Results and Implications for the LHC', CERN, 28 June 2002, `http://sl.web.cern.ch/SL/sli/Scrubbing-2002/Workshop.htm`.

[84] G. Rumolo and F. Zimmermann, *Electron Cloud Instability with Space Charge or Beam Beam*, Proc. Int. Workshop on Two-stream Instabilities in Particle Accelerators and Storage Rings, Tsukuba, 11–14 September, 2001, and CERN-SL-2001-067-AP (2001).

[85] K. Ohmi and A. Chao, *Combined Phenomena of Beam-Beam and Beam Electron Cloud Effects in Circular e^+e^- Colliders*, Phys. Rev. ST Accel. Beams **5**, 101001 (2002).

[86] E. Benedetto et al., *Transverse Monopole Instability Driven by an Electron Cloud?*, Proc. PAC2003, Portland, May 2003, and CERN-AB-2003-036-ABP (2003).

[87] K. Ohmi et al., *Study of Coherent Tune Shift Caused by Electron Cloud in Positron Storage Rings*, Proc. 2nd APAC Conference, Beijing, 2001, and CERN-SL-2001-062-AP (2001).

[88] G. Rumolo, A.Z. Ghalam, T. Katsouleas, C.K. Huang, V.K. Decyk, C. Ren, W.B. Mori, F. Zimmermann, and F. Ruggiero, *Electron cloud effects on beam evolution in a circular accelerator*, Phys. Rev. ST Accel. Beams **6**, 081002 (2003).

[89] A. Ferrari, unpublished (2003).

[90] P. Thieberger et al., *Secondary-Electron Yields and Their Dependence on the Angle of Incidence on Stainless-Steel Surfaces for Three Energetic Ion Beams*, Phys. Rev. A**61**, 042901 (2000).

[91] C. Benvenuti et al., *Vacuum Properties of TiZrV Non-Evaropable Getter Films [for LHC Vacuum System]*, Vacuum **60**, 57–65 (2001).

[92] C. Scheuerlein et al., *The Secondary Electron Yield of TiZr and TiZrV Non-Evaporable Getter Thin Film Coatings*, Appl. Surf. Sci. **172**, 95–102 (2001), and CERN EST/2000-007 (SM) (2000).

[93] B. Henrist et al., CERN Vac. Tech. Note 98-08 (1998).

[94] B. Henrist and C. Scheuerlein, CERN Vac. Tech. Note 98-20 (1998).

[95] A. Rossi, *SPS electron cloud measurements with TiZrV NEG coating*, minutes of the CERN Accelerator Performance Committe meeting of 01.08.2003, `http://ab-div.web.cern.ch/ab-div/Meetings/APC/`.

[96] W. Herr and J. Miles, *A Comparative Study of Beam-beam Tune Footprints for Colliding Beams with a crossing angle and offset vertex in LHC V4.1*, CERN LHC Project Note 04 (1995).

[97] H. Grote and O. Meincke, *Tune footprints for collision optics 5.0*, CERN LHC Project Note 161 (1998).

[98] W. Herr, *Beam-beam issues in the LHC and relevant experience from the SPS proton antiproton collider and LEP*, in CERN LHC Project Report 502 (2001) and Proc. Workshop on Beam-Beam Effects in Circular Colliders, Fermilab, Batavia, IL, USA, 25–28 June 2001, eds. T. Sen and M. Xiao, FERMILAB-CONF-01-390 (2002).

[99] K. Cornelis, M. Meddahi, and R. Schmidt, *The beam-beam effect in the SPS proton antiproton collider for beams with unequal emittances*, CERN SL/90-73 (AP) (1990); W. Herr, *Beam-beam issues in the LHC and relevant experience from the SPS proton antiproton collider and LEP*, Proc. Workshop on 'Beam-Beam Effects in Circular Colliders', Fermilab, Batavia, IL, USA, 25–28 June 2001, eds. T. Sen and M. Xiao, FERMILAB-CONF-01-390 (2002), `http://www-ap.fnal.gov/~meiqin/beambeam01/beambeam01.html`.

[100] H. Grote, F. Schmidt, and L.H.A. Leunissen, *LHC Dynamic Aperture at Collision*, CERN LHC Project Note 197 (1999), Y. Luo and F. Schmidt, *Dynamic aperture studies for LHC optics version 6.2 at collision*, CERN LHC Project Note 310 (2003), see also Y. Luo and F. Schmidt, *Weak-strong beam-beam tracking for LHC v6.1*, CERN LHC Project Report 502 (2001) and Proc. Workshop on 'Beam-Beam Effects in Circular Colliders', Fermilab, Batavia, IL, USA, 25–28 June 2001, eds. T. Sen and M. Xiao, FERMILAB-CONF-01-390 (2002), `http://www-ap.fnal.gov/~meiqin/beambeam01/beambeam01.html`.

[101] Y. Papaphilippou and F. Zimmermann, *Weak-strong beam-beam simulations for the LHC*, in Proc. Workshop on 'Beam-Beam Effects in Large Hadron Colliders' (LHC99), CERN, Geneva, Switzerland, 12–17 April 1999, eds. J. Poole and F. Zimmermann (CERN SL-99-039-AP, 1999), pp. 95–107, see also Phys. Rev. ST Accel. Beams **2**, 104001 (1999) and Y. Papaphilippou and F. Zimmermann, *Estimates of diffusion due to long-range beam-beam collisions*, CERN LHC Project Report 600 (2002) and Phys. Rev. ST Accel. Beams **5**, 074001 (2002).

[102] W. Herr, *Effects of PACMAN bunches in the LHC*, CERN LHC Project Report 39 (1996).

[103] O. Brüning, W. Herr, and R. Ostojic, *A beam separation and collision scheme for IP1 and IP5 at the LHC for optics version 6.1*, CERN LHC Project Report 315 (1999).

[104] O. Brüning, W. Herr, and R. Ostojic, *A beam separation and collision scheme for IP2 and IP8 at the LHC for optics version 6.1*, CERN LHC Project Report 367 (2000).

[105] W. Herr, *Features and implications of different LHC crossing schemes*, CERN LHC Project Report 628 (2003).

[106] B. Muratori, *Study of Offset Collisions and Beam Adjustment in the LHC Using a Strong-Strong Simulation model*, CERN LHC Project Report 593 (2002).

[107] H. Grote, *Comparing beam-beam effects in three LHC injection schemes*, CERN LHC Project Note 267 (2001).

[108] H. Grote and W. Herr, *Self-consistent orbits with beam-beam effects in the LHC*, in CERN LHC Project Report 502 (2001) and Proc. Workshop on 'Beam-Beam Effects in Circular Colliders', Fermilab, Batavia, IL, USA, 25–28 June 2001, eds. T. Sen and M. Xiao, FERMILAB-CONF-01-390 (2002).

[109] L. Vos, *Effect of very low frequency ground motion on the LHC*, in Proc. Workshop on 'Beam-Beam Effects in Large Hadron Colliders' (LHC99), CERN, Geneva, Switzerland, 12–17 April 1999, eds. J. Poole and F. Zimmermann (CERN SL-99-039-AP, 1999), pp. 91–94.

[110] H. Grote and W. Herr, *Nominal and ultimate luminosity performance of the LHC*, CERN LHC Project Note 275 (2002).

[111] K. Yokoya et al., *Tune shift of coherent beam-beam oscillations*, Part. Acc. **27**, 181 (1990).

[112] Y. Alexahin, *On the Landau damping and decoherence of transverse dipole oscillations in colliding beams*, Part. Acc. **59**, 43 (1996).

[113] M.P. Zorzano and F. Zimmermann, *Coherent beam-beam oscillations at the LHC*, CERN LHC Project Report 314 (1999) and Phys. Rev. ST Accel. Beams **3**, 044401 (2000).

[114] W. Herr, M.P. Zorzano, and F. Jones, *A hybrid fast multipole method applied to beam-beam collisions in the strong-strong regime*, Phys. Rev. ST Accel. Beams **4**, 054402 (2001).

[115] Y. Alexahin, H. Grote, W. Herr and M.P. Zorzano, *Coherent beam-beam effects in the LHC*, CERN LHC Project Report 466 (2001).

[116] Y. Alexahin, *A study of the coherent beam-beam effect in the framework of the Vlasov perturbation theory*, Nucl. Inst. Meth. **A 380**, 253 (2002).

[117] Y. Alexahin and M.P. Zorzano, *Excitation of coherent beam-beam resonances for beams with unequal tunes in the LHC*, CERN LHC Project Note 226 (2000).

[118] W. Herr and M.P. Zorzano, *Coherent dipole modes for multiple interaction regions*, CERN LHC Project Report 461 (2001).

[119] W. Herr and R. Paparella, *Landau damping of coherent modes by overlap with synchrotron sidebands*, CERN LHC Project Note 304 (2002).